The EDGE-CALIFA survey: self-regulation of star formation at kpc scales

J Barrera-Ballesteros, S Sánchez, T Heckman, T Wong, A Bolatto, E Ostriker, E Rosolowsky, L Carigi, S Vogel, R Levy, et al.

Monthly Notices
of the
ROYAL ASTRONOMICAL SOCIETY

MNRAS **503,** 3643–3659 (2021)
Advance Access publication 2021 March 13

doi:10.1093/mnras/stab755

The EDGE-CALIFA survey: self-regulation of star formation at kpc scales

J. K. Barrera-Ballesteros [1]★ S. F. Sánchez,[1]★ T. Heckman,[2]★ T. Wong,[3] A. Bolatto,[4] E. Ostriker,[5] E. Rosolowsky [6], L. Carigi,[1] S. Vogel,[4] R. C. Levy [4], D. Colombo,[7] Yufeng Luo [3], Yixian Cao[3,8] and the EDGE-CALIFA team

[1]*Instituto de Astronomía, Universidad Nacional Autónoma de México, A.P. 70-264, 04510 México, D.F., México*
[2]*Department of Physics and Astronomy, Johns Hopkins University, Bloomberg Center, 3400 N. Charles St, Baltimore, MD 21218, USA*
[3]*Department of Astronomy, University of Illinois, Urbana, IL 61801, USA*
[4]*Department of Astronomy, University of Maryland, College Park, MD 20742, USA*
[5]*Department of Astrophysical Sciences, University of Princeton, Peyton Hall, 4 Ivy Lane, Princeton, NJ 08544, USA*
[6]*Department of Physics, University of Alberta, 4-181 CCIS, Edmonton, AB T6G 2E1, Canada*
[7]*Max-Planck-Institut für Radioastronomie, Auf dem Hügel 69, D-53121 Bonn, Germany*
[8]*Aix Marseille Université, CNRS, LAM (Laboratoire d'Astrophysique de Marseille), F-13388 Marseille, France*

Accepted 2021 March 5. Received 2021 February 11; in original form 2020 November 16

ABSTRACT

The processes that regulate star formation are essential to understand how galaxies evolve. We present the relation between star formation rate density, $\Sigma_{\rm SFR}$, and hydrostatic mid-plane pressure, $P_{\rm h}$, for 4260 star-forming regions of kpc size located in 96 galaxies included in the EDGE-CALIFA survey covering a wide range of stellar masses and morphologies. We find that these two parameters are tightly correlated, showing a smaller scatter in comparison to other star-forming relations. A power law, with a slightly sublinear index, is a good representation of this relation. Its residuals show a significant anticorrelation with both stellar age and metallicity whereas the total stellar mass may also play a secondary role in shaping the $\Sigma_{\rm SFR}$–$P_{\rm h}$ relation. For actively star-forming regions, we find that the effective feedback momentum per unit stellar mass (p_*/m_*), measured from the $P_{\rm h}/\Sigma_{\rm SFR}$ ratio increases with $P_{\rm h}$. The median value of this ratio for all the sampled regions is larger than the expected momentum just from supernovae explosions. Morphology of the galaxies, including bars, does not seem to have a significant impact in the $\Sigma_{\rm SFR}$–$P_{\rm h}$ relation. Our analysis indicates that local $\Sigma_{\rm SFR}$ self-regulation comes mainly from momentum injection to the interstellar medium from supernovae explosions. However, other mechanisms in disc galaxies may also play a significant role in shaping the $\Sigma_{\rm SFR}$ at kpc scales. Our results also suggest that $P_{\rm h}$ is the main parameter that modulates star formation at kpc scales, rather than individual components of the baryonic mass.

Key words: techniques: imaging spectroscopy – galaxies: evolution – galaxies: fundamental parameters – galaxies: star formation.

1 INTRODUCTION

The understanding of the physical conditions that lead to the formation of new stars in galaxies is essential to understand their formation and evolution. There are basically two physical scenarios that drive the star formation in disc galaxies (see a review in Kennicutt & Evans 2012). In the first scenario, the star formation is mostly controlled by the properties and amount of the interstellar medium (ISM). In this so-called 'bottom-up' picture, the local star formation rate (SFR) is controlled completely by the amount of dense gas and structure of the molecular clouds (e.g. Krumholz & McKee 2005). On the other hand, in the so-called 'top-down' scenario, local star formation is controlled largely by global dynamical events and dynamical time-scales (e.g. Silk 1997). In the latter scenario, variations of star formation is controlled by gravitational instabilities in the disc rather than cooling of molecular clouds, with no distinction between densities regimes of the molecular clouds that can affect the amount of newly formed stars. Another model that emerge from these two views is the self-regulation star formation scenario in which the hydrostatic pressure from the baryonic component balances the feedback from newly formed massive stars reaching an equilibrium (e.g. Cox 1981; Dopita 1985; Silk 1997).

Using data from the PHANGS survey, Sun et al. (2020) found that the dynamical pressure (i.e. the pressure due to self-gravity and external disc gravity) is in equilibrium with the turbulent pressure for most of their sampled molecular clouds located in nearby star-forming galaxies. Different mechanisms can be considered that could explain such equilibrium including momentum flux injection to the interstellar medium (ISM) from stellar feedback (including supernovae explosions, stellar winds, and radiation, e.g. Thompson, Quataert & Murray 2005; Ostriker & Shetty 2011; Faucher-Giguère, Quataert & Hopkins 2013) or/and gravitational instabilities (e.g. Ibáñez-Mejía et al. 2017; Krumholz & Burkhart 2016). The injection of momentum due to stellar feedback into the ISM is a rather sporadic

★ E-mail: jkbarrerab@astro.unam.mx (JKB-B); sfsanchez@astro.unam.mx (SFS); theckman@jhu.edu (TH)

and very localized event that may not occur in every single location of the galaxy where molecular gas is available. Therefore, in the self-regulated framework, a star-forming galaxy can be considered as a quasi-steady-state system (Ostriker, McKee & Leroy 2010; Ostriker & Shetty 2011). The equilibrium between the pressure and the star formation feedback has to be considered on spatial scales significantly larger than the typical size of giant molecular clouds (few tenths of pc) and temporal scales larger than a cycle of star formation. Numerical simulations suggest that these scales are of the order of few kpc and few hundreds of Myr (e.g. Kim, Ostriker & Raileanu 2017; Semenov, Kravtsov & Gnedin 2017; Orr et al. 2018).

Recently, the relation between the star formation surface density and the pressure at kpc scales has been investigated extensively in different surveys including star-forming galaxies. Using a sample of 23 dwarf and disc galaxies included in the HERACLES survey, Leroy et al. (2008) found a strong correlation between these two observables for radial bins. Herrera-Camus et al. (2017) and Sun et al. (2020) found similar results using spatially resolved data set from samples of 31 and 28 star-forming galaxies in the nearby Universe ($D \lesssim 30$ Mpc) included in the KINGFISH and PHANGS surveys, respectively. In general, the strong correlation between the star formation surface density ($\Sigma_{\rm SFR}$) and the pressure is in agreement with a linear relation (i.e. power-law index close to 1). Theory and numerical simulations suggest that this could be the case in the scenario in which supernovae feedback is the main supplier of pressure against the hydrostatic pressure (e.g. Ostriker & Shetty 2011; Kim, Ostriker & Kim 2013).

At those kpc scales, $\Sigma_{\rm SFR}$ exhibits a strong correlation with the surface gas density ($\Sigma_{\rm gas}$) in star-forming galaxies (also known as Schmidt–Kennicutt relation, see rSK; Kennicutt & Evans 2012, and reference therein). On the other hand, Integral Field Spectroscopy (IFS) used in large samples of star-forming galaxies has made clear the strong relation between $\Sigma_{\rm SFR}$ and the stellar component of the baryonic mass at kpc scales, Σ_{*}, known as the resolved star formation main sequence (rSFMS, see a review in Sánchez 2020, and references therein). Both baryonic components, tracing the local gravitational potential or similarly the hydrostatic pressure, may provide a better estimate of $\Sigma_{\rm SFR}$ at kpc scales (e.g. Barrera-Ballesteros et al. 2021). Therefore we would like to explore whether a star-forming scaling relation that uses both components of the baryonic mass (like the hydrostatic mid-plane pressure, $P_{\rm h}$) provides a better description of $\Sigma_{\rm SFR}$ than those relations using individual components of the baryonic mass.

Among the recent efforts to explore the local properties of galaxies in the nearby Universe, the CARMA Extragalactic Database for Galaxy Evolution (EDGE) survey (Bolatto et al. 2017) has mapped the molecular gas in 126 galaxies observed IFS data from the Calar Alto Legacy Integral Field Area (CALIFA) survey (Sánchez et al. 2012). This yields a data set that allows us not only to study the interplay of the molecular gas with other observables derived from the optical spectra at kpc scales, but also to explore the impact of the global/integrated properties in the derived local scaling relations. The EDGE-CALIFA survey overcomes the so-called 'cosmic variance' problems, meaning that it samples a sufficient volume of the Universe to truly represent the relations at local scales (e.g. Diemer et al. 2019). Among other results, this survey has improved our understanding of how the molecular gas depletion time changes across the extension of galaxies (Utomo et al. 2017), on how different local and global parameters affect $\Sigma_{\rm SFR}$ using a multilinear approach (Dey et al. 2019), and on how we can characterize the molecular gas at kpc scales using the optical extinction (Barrera-Ballesteros et al. 2020). Using the EDGE-CALIFA spatially resolved data set, we explore in this paper the relation between $\Sigma_{\rm SFR}$ and $P_{\rm h}$. We find that these two parameters are strongly correlated, suggesting that star formation at kpc scales, in a significant fraction of regions located in galaxies in the nearby Universe, is consistent with the self-regulation scenario (e.g. Elmegreen 1989; Silk 1997). We explore the impact of local and global observables in this relation as well as its role in comparison to other star-forming scaling relations. This paper is organized as follows. In Section 2, we present the spatially resolved and ancillary data used in this study that is available in the `edge_pydb` data base (Wong et al. in preparation). In Section 3, we show the main results of this paper. In Section 4, we discuss these results. Finally, in Section 5, we present the main conclusions of this paper.

2 DATA AND ANALYSIS

2.1 The CALIFA and EDGE surveys

Here we provide a brief description of the optical IFS CALIFA and the molecular gas EDGE surveys, respectively. Observations from both surveys comprise the core data sets that we use in this study to perform our analysis.

The CALIFA survey (Sánchez et al. 2012) provides IFS data for more than 600 galaxies in the nearby Universe ($0.005 < z < 0.03$) using the PMAS/PPAK Integral Field Unit (IFU) instrument (Roth et al. 2005) mounted at the 3.5-m telescope of the Calar Alto Observatory. The instrument consists of 331 fibres of 2.7-arcsec diameter each, concentrated in a single hexagon bundle covering a field of view (FoV) of $\sim$1 arcsec^2 with a filling factor of $\sim$60 per cent . To provide a full coverage of the FoV a three-point dithering is performed. The average resolution of this instrument is $\lambda/\Delta\lambda \sim 850$ at $\sim$5000 Å with a typical wavelength range from 3745 to 7300 Å. The isophotal diameter of CALIFA galaxies are in the range $45 \lesssim D_{25} \lesssim 80$ arcsec in the SDSS (Sloan Digital Sky Survey) *r*-band (Walcher et al. 2014). The data reduction is performed by a pipeline designed specifically for the CALIFA survey. The final data cube for each galaxy consists of more than 5000 spectra with a sampling of 1×1 arcsec^2 per spaxel. The reduction process is described in detail in Sánchez et al. (2012); improvements on the reduction pipeline as well as extensions to the original sample (reaching a total of 834 galaxies) are presented by Husemann et al. (2013), García-Benito et al. (2015), and Sánchez et al. (2016c).

The EDGE survey obtained millimeter-wave interferometric observations for a sample of 126 galaxies included in the CALIFA survey. These observations were carried out at the Combined Array for Millimeterwave Astronomy (CARMA; Bock et al. 2006). The EDGE survey provides the first effort to combine resolved CO data with IFS optical data for a significant sample of galaxies representative of the local Universe. We present a brief description of the survey here; see Bolatto et al. (2017) for a detailed description. Galaxies were observed using half-beam-spaced seven-point hexagonal mosaics yielding a half-power FoV of radius $\sim$50 arcsec. Each galaxy has been observed in both the E and D-array configuration with integration times typically of 40 min and 3.5 h, respectively. The typical resolution for each configuration is 8 and 4 arcsec, respectively. The final maps combined the E and D array observations resulting in a velocity resolution of 20 km s^{-1} with a typical angular resolution of 4.5 arcsec and typical rms sensitivity of 30 mK at the velocity resolution. Assuming a Milky Way constant CO-to-H_2 conversion factor ($\alpha_{\rm CO} = 4.3\,{\rm M}_{\odot}({\rm K\,km\,s^{-1}\,pc^2})^{-1}$; Bolatto, Wolfire & Leroy 2013), the survey is sensitive to an H_2 surface mass density of $\sim$ 4–110 M$_{\odot}$ pc^{-2} (averaged over an $\sim$1.5-kpc scale). The data cubes are smoothed and then masked in order to distinguish CO

signal from noise and to reach a higher signal to noise ratio (see more details in Bolatto et al. 2017).

2.2 The edge_pydb data base

As we show above, the spatially resolved data set from the IFU CALIFA survey and the data set from the CO millimeter obtained from CARMA array are relatively different in terms of FoV coverage, spatial resolutions, and spatial sampling. The edge_pydb data base has been created as a homogeneous source of optical and millimeter maps and data for the 126 EDGE galaxies to be used in a flexible python environment that allows a simple yet robust exploration of the EDGE-CALIFA data set. This data base also provides an integration of external properties with the spatially resolved information. A detailed description of the data base can be found in Wong et al. (in preparation). Here we highlight its main features and the data used in this analysis.

This data base provides different estimates of the CO moments from the CARMA observations. The data base also provides a smoothed and masked version of the CARMA CO datacubes. The CO datacubes are integrated in the velocity axis to obtain the surface brightness maps (smo table). Both CALIFA and EDGE data sets are convolved to the same spatial resolution (i.e. 7 arcsec). Then the PIPE3D data analysis pipeline (Sánchez et al. 2016a,b) is run over the convolved optical datacubes, resulting in two-dimensional maps of optical properties with the same resolution as the CO surface brightness maps. By fitting the stellar continuum (using a single stellar population fitting, SSP, adopting a Salpeter 1955 initial mass function, IMF, and the emission lines for each of the spaxels in each datacube, this pipeline extracts two-dimensional maps of a given stellar or ionized gas observable. The maps are sampled on a square grid spaced by 3 arcsec in RA and Dec. after interpolation to the CARMA WCS. The grid is shifted so that the reference pixel from the original data cube is retained. The tables with ancillary data include information from the LEDA and NED data bases, IR photometry from the *WISE* survey, among others. The data base also include the information from integrated properties derived from the CO and optical datacubes. For each of the galaxies in this study, we use the values from the data base of: the total molecular gas mass, ($M_{\rm mol}$), the total stellar mass (M_*), the integrated SFR, the effective radius ($R_{\rm eff}$), the stellar scale length ($l_{\rm s}$), the minor-major axial ratio (b/a), and the morphology. The reader is addressed to Wong et al. (in preparation) for a detailed description on how these observables are derived or from which data base they have been obtained.

2.3 Derived quantities

We use the maps of the molecular gas density, $\Sigma_{\rm mol}$, for each galaxy from the edge_pydb data base. These maps are obtained by converting the CO surface brightness maps from the smo list into molecular gas mass density maps using a constant CO-to-H_2 conversion factor following (Bolatto et al. 2013, $\alpha_{\rm CO} = 4.3\,{\rm M}_\odot({\rm K\,km\,s^{-1}\,pc^2})^{-1}$). This factor includes the mass contribution from helium (below we also estimate a variable conversion factor).

The edge_pydb data base provides all the maps from both the stellar continuum and the ionized gas components derived from the PIPE3D pipeline. From the fitting of the stellar continuum, we use the stellar surface mass density map (Σ_*), the stellar age and metallicity ([Z/H]), and the stellar velocity dispersion (σ_*) for each of the sampled regions. From the analysis of emission lines of the ionized gas, we use the integrated flux maps of Hα, Hβ, [O III] and [N II] emission lines. We also use the equivalent width map of the Hα emission line (EW(Hα), see details in Sánchez et al. 2016b). From these emission-line fluxes, we derive the Balmer decrement ratio (Hα/Hβ). From this ratio and the Hα emission line, we obtain the extinction-corrected SFR surface density map, $\Sigma_{\rm SFR}$ (Kennicutt 1998a). All the surface densities are corrected by the galaxy's inclination following Barrera-Ballesteros et al. (2016). For this study, we adapted both the $\Sigma_{\rm SFR}$, and Σ_*densities to a Kroupa IMF. This is equivalent to multiply these quantities in the data base (Salpeter IMF) by a factor of 0.61 (see Madau & Dickinson 2014). As proxy for the inclination, we use the b/a axial ratio. The typical relative error of $\Sigma_{\rm mol}$, Σ_*, and $\Sigma_{\rm SFR}$ are ∼0.28, 0.15, and 0.20 dex, respectively.

We follow Elmegreen (1989) to derive for each region the mid-plane hydrostatic pressure[1] ($P_{\rm h}$):

$$P_{\rm h} = \frac{\pi}{2}\, G\, \Sigma_{\rm gas} \left(\Sigma_{\rm gas} + \frac{\sigma_{\rm gas}}{\sigma_{*,z}}\, \Sigma_* \right), \tag{1}$$

where G is the gravitational constant, $\Sigma_{\rm gas}$ and $\sigma_{\rm gas}$ are the total gas surface mass density (molecular and atomic $\Sigma_{\rm gas} = \Sigma_{\rm mol} + \Sigma_{\rm H\,I}$) and the total gas velocity dispersion, respectively, and $\sigma_{*,z}$ is the stellar velocity dispersion in the axis perpendicular to the disc. Since we do not have direct observations of the atomic gas density distribution for these galaxies, to derive the best fit of the $\Sigma_{\rm SFR}$–$P_{\rm h}$ relation in Section 3.1 we run a Monte Carlo simulation assuming 1000 realizations with different values of $\Sigma_{\rm H\,I}$ within a normal distribution centred at $\Sigma_{\rm H\,I} = 7\ {\rm M}_\odot\ {\rm pc}^{-2}$ and with a standard deviation of $2\ {\rm M}_\odot\ {\rm pc}^{-2}$. This range of values is representative of the atomic gas densities found in normal star-forming galaxies for the range of total stellar masses and morphologies probed by our sample (e.g. Bigiel et al. 2008; Bigiel & Blitz 2012; Wang et al. 2014). The value of $P_{\rm h}$ for each region presented in this study is thus the average of the above realizations. We adopt a constant value of the total gas velocity dispersion $\sigma_{\rm gas} = 11\ {\rm km\,s^{-1}}$. This value is within the range of typical velocity dispersions found in disc galaxies for both components of the cold gas in the nearby Universe (e.g. Caldú-Primo et al. 2013; Levy et al. 2018) and have been adopted in different studies of the $\Sigma_{\rm SFR}$–$P_{\rm h}$ relation(e.g. Leroy et al. 2008; Sun et al. 2020). To estimate $\sigma_{*,z}$, we follow Leroy et al. (2008), Zheng et al. (2013). By assuming a relation between this dispersion and the disc scale height ($h_{\rm s}$) and the stellar mass surface density for an isothermal disc (van der Kruit 1988), we have

$$\sigma_{*,z} = \sqrt{2\,\pi\, G\, \Sigma_* h_{\rm s}}, \tag{2}$$

here we assume that the EDGE-CALIFA galaxies follow the ratio $l_{\rm s}/h_{\rm s} = 7.3$, where $l_{\rm s}$ is the disc stellar scale length (Kregel, van der Kruit & de Grijs 2002; Sun et al. 2020). In turn, we relate the stellar scale length $l_{\rm s}$ of the disc to the effective radius of the galaxies in units of pc by adopting $l_{\rm s} = R_{\rm eff}/1.68$ (i.e. assuming a Sersic profile with $n = 1$, Graham & Driver 2005). We adopt this relation in order to provide an estimation of $l_{\rm s}$ in larger samples of galaxies where only $R_{\rm eff}$ has been determined. In Appendix A, we compare the $\sigma_{*,z}$ ratio assuming different estimations of $l_{\rm s}$.

In Section 3.4, we study the impact of a variable $\alpha_{\rm CO}$ conversion factor in the estimation of the hydrostatic mid-plane pressure. We use equation (7) from Colombo et al. (2020) to estimate this variable conversion factor:

$$\alpha_{\rm CO}(Z', \Sigma_*) = 2.9 \exp\left(\frac{0.4}{Z'}\right) \left(\frac{\Sigma_*}{100\,{\rm M}_\odot\,{\rm pc}^{-2}}\right)^{-\gamma}, \tag{3}$$

[1]Note that we use the traditional term 'hydrostatic', even though the gas in the ISM is not static, with the majority of the pressure associated with turbulence.

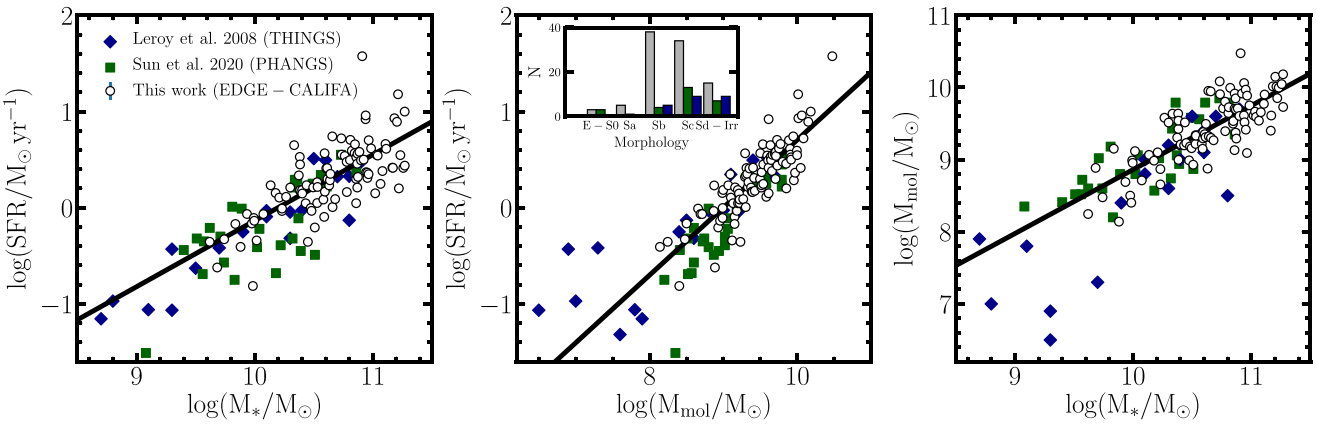

Figure 1. Comparison of the 96 EDGE-CALIFA galaxies used in this study (empty circles) with different samples where the spatially resolved $\Sigma_{\rm SFR}$–$P_{\rm h}$ relation has been derived. Blue diamonds, and green squares represent the samples from the THINGS (Leroy et al. 2008) and PHANGS surveys (Sun et al. 2020), respectively. The samples are presented in the SFR–M_* (left-hand panel), the SFR–$M_{\rm mol}$ (middle panel), and the M_*–$M_{\rm mol}$ planes (right-hand panel). The solid lines represent the best linear fits to the data points in our sample. The inset in the middle panel shows the distribution of morphologies for this sample (empty bins), the THINGS+HERACLES (blue bins), and the PHANGS (green bins) surveys, respectively. Our sample covers a significant dynamic range in global properties for a variety of morphological types, which is essential to study the impact of global parameters on the $\Sigma_{\rm SFR}$–$P_{\rm h}$ relation at kpc scales.

where $\alpha_{\rm CO}(Z',\ \Sigma_*)$ is in units of $\rm M_\odot(K\,km\,s^{-1}\,pc^2)^{-1}$, Z' is the ionized gas metallicity relative to the solar one, and $\gamma = 0.5$ where $\Sigma_* > 100\,\rm M_\odot\,pc^{-2}$ and $\gamma = 0$ otherwise. This is a variation of the variable conversion factor derived in Equation 31 by Bolatto et al. (2013). Following Colombo et al. (2020), we assume that the total density in our regions is dominated by $\Sigma_*(\Sigma_{\rm total} \sim \Sigma_*)$, also that the Giant Molecular Cloud (GMC) molecular gas surface density in units of 100 $\rm M_\odot\ pc^{-2}$ is equal to 1 (i.e. we assume that $\Sigma_{\rm mol}$ for GMCs are largely consistent with this density). The ionized gas metallicity is obtained by using the strong-lines calibrator derived by Marino et al. (2013):

$$12 + \log(\rm O/H) = 8.533 - 0.214 \left(\frac{[\rm O\,III]}{\rm H\,\beta} \times \frac{\rm H\,\alpha}{[\rm N\,II]} \right). \quad (4)$$

To provide a reliable comparison with the literature, in Section 3.5, instead of $P_{\rm h}$, we use a slightly different estimate of the dynamical equilibrium pressure, $P_{\rm DE}$. Following Kim, Kim & Ostriker (2011) and Sun et al. (2020), $P_{\rm DE}$ is given by

$$P_{\rm DE} = \frac{\pi G}{2} \Sigma_{\rm gas}^2 + \Sigma_{\rm gas} \sqrt{2 G \rho_*}\, \sigma_{\rm gas,z}, \quad (5)$$

where ρ_* is the mid-plane stellar volume density (Sun et al. 2020, see their Equation 13). Here, $\sigma_{\rm gas,\,z}$ is the velocity dispersion of the gas perpendicular to the disc, and we adopt a value of 11 $\rm km\,s^{-1}$ as above. Sun et al. (2020) noted that this estimate can slightly increase the measurement of $P_{\rm DE}$ by a factor at most of ∼0.2 dex in comparison to those dynamical pressures derived directly from their observations. We perform a similar analysis as in Section 3.1, this is, we assume 1000 different realizations of $\Sigma_{\rm H\,I}$. We presented in this paper the averaged values of $P_{\rm DE}$ from those realizations.

The `edge_pydb` data base provides the information derived from the CALIFA and EDGE data for over ∼16 000 individual regions located in the 126 galaxies included the survey. For the analysis in this paper, we select those star-forming regions with the most reliable estimations of the considered observables. This is, regions where $\Sigma_{\rm mol}$, H α, and H β have values larger than three times their errors as well as non-zero estimates of their Σ_* and their $\Sigma_{\rm SFR}$ and EW(H α)> 6Å. This selection yields a total of 4260 regions located in 96 galaxies. In Fig. 1, we compare the EDGE-CALIFA galaxies used in this study with other angular-resolved samples used to estimate the $\Sigma_{\rm SFR}$–$P_{\rm DE}$ relation in the SFR–M_*, in the SFR–$M_{\rm mol}$, and in the M_*–$M_{\rm mol}$ planes. The dynamical range of our sample in these three observables is wide, covering approximately two orders of magnitude for each of them. In comparison to our sample, the THINGS sample (Leroy et al. 2008) covers a range of low-mass galaxies, whereas the 28 galaxies from the PHANGS sample from Sun et al. (2020) cover a similar range of properties as our sample ,[2] however the EDGE-CALIFA galaxies includes a wide range in morphologies (see the inset in the middle panel of Fig. 1). In Section 3.3 we explore how the radial distribution of the $\Sigma_{\rm SFR}$–$P_{\rm h}$ relation varies for galaxies with different global star formation activity and global gas fraction derived from the best fits of the above relations (black lines in each panel of Fig. 1). For our sample of galaxies in the SFR–M_*, the SFR–$M_{\rm mol}$, and in the M_*–$M_{\rm mol}$ planes, these fits correspond to: $\log(\rm SFR/M_\odot\,yr^{-1}) = -7.0 + 0.68\,\log(M_*/M_\odot)$, $\log(\rm SFR/M_\odot\,yr^{-1}) = -6.3 + 0.70\,\log(M_{\rm mol}/M_\odot)$, and $\log(M_{\rm mol}/M_\odot) = 0.88\,\log(M_*/M_\odot)$, respectively. Furthermore, in Section 3.5, we compare the estimate of the $\Sigma_{\rm SFR}$–$P_{\rm DE}$ relation using our sample and those derived using samples with resolved measurements.

3 RESULTS

3.1 The $\Sigma_{\rm SFR}$–$P_{\rm h}$ relation at kpc scales for the EDGE-CALIFA galaxies.

In Fig. 2, we show the $\Sigma_{\rm SFR}$–$P_{\rm h}$relation for our data set that includes 4260 regions located in 96 EDGE-CALIFA galaxies. The hydrostatic mid-plane pressure covers approximately four orders of magnitude whereas $\Sigma_{\rm SFR}$ covers approximately three orders of magnitude. On a log-log scale, $\Sigma_{\rm SFR}$ increases linearly with $P_{\rm h}$, resulting in a strong correlation (Pearson correlation coefficient of $r = 0.85$). Similar but

[2]Estimates of $M_{\rm mol}$ for the PHANGS survey have been kindly provided by A. K. Leroy (private communication). Full details will be available in Leroy et al. (in preparation). SFR, and M_* values are taken from the website: https://sites.google.com/view/phangs/home/sample

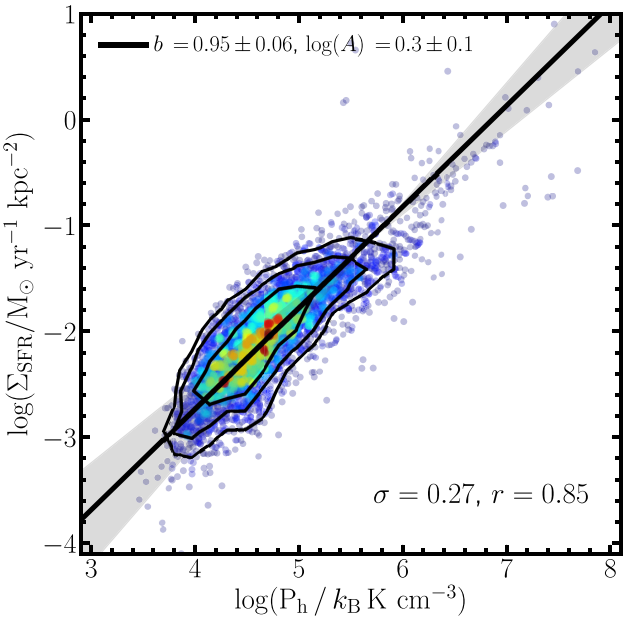

Figure 2. The Σ_{SFR}–P_h relation for 4260 star-forming regions included in 96 galaxies from the EDGE-CALIFA survey. The data points are colour-coded according to the density of points. Inwards, the black contours enclose 90, 80, and 50 per cent of the sample. The solid line represents the best ODR linear fit. The shaded area represents the uncertainty of the fit due to the assumed values of Σ_{HI}. The tightness of the relation is indicated by the small standard deviation (σ), whereas r represents the Pearson correlation coefficient.

smaller correlation coefficients have also been observed in other star-forming scaling relation at kpc scales (e.g. the rSFMS or the rSK; Cano-Díaz et al. 2016, 2019; Lin et al. 2019)

To obtain the best parameters that represent the Σ_{SFR}–P_h relation, we fit the following relation to our data set using an orthogonal distance regression (ODR) fitting technique:

$$\frac{\Sigma_{SFR}}{10^{-3} M_\odot\ yr^{-1}\ kpc^{-2}} = A \left(\frac{P_h}{10^4\ k_B\ K\ cm^{-3}} \right)^b, \quad (6)$$

the fitting procedure was repeated 1000 times for each of the different realizations performed to take into account our lack of knowledge of the Σ_{HI} distribution (see Section 2.3). The shaded area in Fig. 2 represents the best fits from these realizations and the black solid line represents their median. Therefore, the reported values of the fit are obtained from this average while their uncertainties come from the scatter of these realizations ($b = 0.95 \pm 0.06$ and $A = 0.3 \pm 0.1$). We also perform an ordinary least-squares (OLS) fit to the average values. We find a slightly flatter relation in comparison to the one derived using the ODR fit ($b = 0.83 \pm 0.04$ and $A = 0.37 \pm 0.05$). In Section 3.5, we compare these slopes with recent results for regions at subkpc scales. The scatter of the residuals – measured from their standard deviation, σ – is small compared to other star-forming scaling relations ($\sigma = 0.27$; see a comparison in Section 3.2). We are interested in exploring how other local and global parameters affect this relation. In Sections 3.2 and 3.3, we study how the residuals from the best fit of this relation correlate with other observables. In Section 4, we discuss the possible different scenarios that can explain the sublinear slope exhibited by this relation.

3.2 Impact of local parameters in the Σ_{SFR}–P_h relation

In the last decade, it has become evident that most of the star-forming scaling relations derived for integrated properties are also observable at kpc scales (for a recent review see Sánchez 2020). Recent studies have also shown that scatter of the star-forming scaling relations is modulated by different local observables (Ellison et al. 2018, 2020). In the previous section, we showed that Σ_{SFR} strongly correlates with P_h. Furthermore, this relation is tight, exhibiting a similar scatter in comparison to other star-forming scaling relations (~ 0.25 dex). In this section, we explore how the Σ_{SFR}–P_h relation compares with the three scaling local relations that correlate Σ_{SFR} , Σ_*, and Σ_{mol} among them at kpc scales. Then we explore how the Σ_{SFR}–P_h relation is modulated by other stellar properties such as the age, metallicity, and their velocity dispersion.

Using a sample of galaxies included in the ALMAQuest survey, Lin et al. (2019) found that within star-forming galaxies Σ_{SFR} , Σ_*, and Σ_{gas} closely correlate with each another. On the one hand, Σ_{SFR} correlates with Σ_*(resolved star formation main sequence, rSFMS; see also Sánchez et al. 2012; Wuyts et al. 2011; Cano-Díaz et al. 2016, 2019), and with Σ_{mol} (resolved Schmidt–Kennicutt relation, rSK; see also Bigiel et al. 2008). On the other hand, Σ_{mol} also correlates with Σ_* (rMGMS; see also Barrera-Ballesteros et al. 2020). We derive these scaling relations using our data set from the EDGE-CALIFA survey. The following are the best relations presented in Sánchez et al. (2021) for this survey: the rSK relation,

$$\log\left(\frac{\Sigma_{SFR}}{M_\odot\ yr^{-1} pc^{-2}}\right) = 0.98\ \log\left(\frac{\Sigma_{mol}}{M_\odot\ pc^{-2}}\right) - 9.01, \quad (7)$$

the rSFMS,

$$\log\left(\frac{\Sigma_{SFR}}{M_\odot\ yr^{-1} pc^{-2}}\right) = 1.02\ \log\left(\frac{\Sigma_{*}}{M_\odot\ pc^{-2}}\right) - 10.10, \quad (8)$$

and the resolved molecular gas main sequence (rMGMS),

$$\log\left(\frac{\Sigma_{mol}}{M_\odot\ pc^{-2}}\right) = 0.93\ \log\left(\frac{\Sigma_{*}}{M_\odot\ pc^{-2}}\right) - 0.91, \quad (9)$$

their typical scatter is of the order of $\sigma \sim 0.25$ dex (see details in Sánchez et al. 2021). For each of these relation, we derive their residuals (i.e. for each star-forming region, the distance in the y-direction between the best fit and the data point). In each of the panels in Fig. 3, we plot these residuals against the one derived from the best fit of the Σ_{SFR}–P_h relation (ΔSFHP): the residuals of the rSK (ΔSK, left-hand panel), the residuals of the rSFMS (ΔSFMS, middle panel), and the residuals of the rMGMS (ΔMGMS, left-hand panel). In principle, ΔSK and ΔSFMS quantify the lack (or excess) of Σ_{SFR} for a given Σ_{gas} and Σ_*, respectively, whereas the ΔMGMS measures the lack or excess of Σ_{mol} for a given Σ_*.

We find that ΔSFMS, and ΔSK correlate with ΔSFHP. This is supported by their Pearson correlation coefficients ($r = 0.95$ and 0.54, respectively). Even more, these two residuals increases linearly with ΔSFHP following a one-to-one relation (solid lines in Fig. 3). This may suggest, that for a given P_h, the variations in Σ_{SFR} are tightly correlated to those variations expected from the rSK and rSFMS. The smaller scatter observed in the left-hand panel of Fig. 3 compared to the one observed in middle panel may indicate that ΔSK has a larger impact in setting Σ_{SFR} for a given P_h. In comparison to the previous correlations, the residuals of the molecular gas main sequence, ΔMGMS, weakly anticorrelates with ΔSFHP($r = -0.31$, right-hand panel of Fig. 3). The lack of a strong correlation between these residuals suggests the small impact that the gas fraction has in modulating the star formation at kpc scales in comparison to the stellar and gas surface densities.

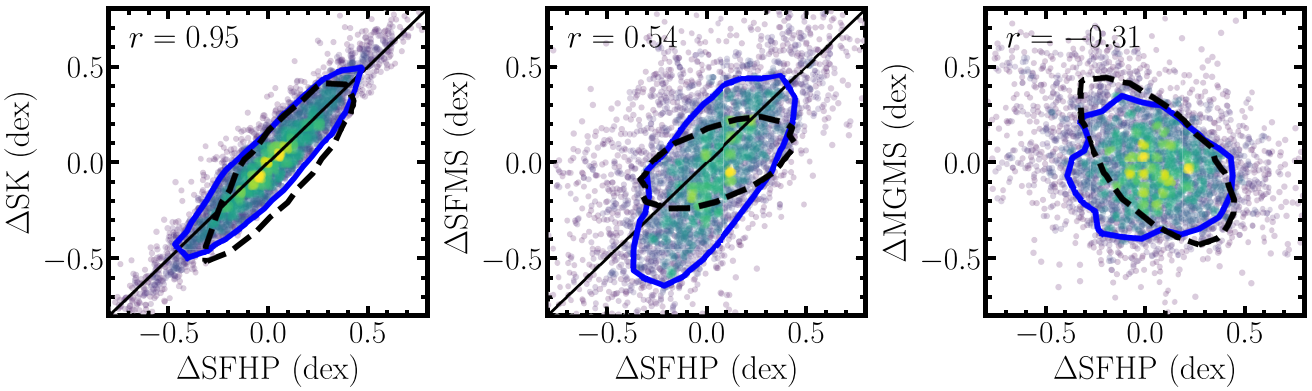

Figure 3. The correlation between the residuals of different scaling relations with those derived from the $\Sigma_{\rm SFR}$–$P_{\rm h}$ relation, ΔSFHP. Left-hand panel: the residuals of the Schmidt–Kennicutt law (ΔSK). Middle panel: The residuals of the rSFMS (ΔSFMS). Right-hand panel: the residuals of the molecular gas main sequence (ΔMGMS). The number in each panel represents the Pearson correlation coefficient. Solid lines in left and middle panels represent a one-to-one relation. In each panel, the blue solid contour encloses ∼64 per cent of the sample while the black dashed contour represents the same fraction for those residuals estimated from mock data assuming a constant scatter around best-fitting scaling relations (see details in Section 3.2). This comparison suggests that correlations between residuals are mostly explained by the strong covariance of the quantities defined in each axis.

Mathematically speaking, the observables from which the previous scaling relations are made of (i.e. the rSK, the rSFMS, and the rMGMS) are the same observables used to derive the $\Sigma_{\rm SFR}$–$P_{\rm h}$ relation. Therefore, the correlations among the residuals we find in Fig. 3 can be induced by the strong covariance among those observables. To test the impact of their covariances in the relations of the residuals, in Appendix B, we build the same relations among residuals using a mock data set by considering the best fits of the scaling relations (i.e. equations 7–9) and assuming the typical scatter from the observables. In each panel of Fig. 3, the blue contour encloses ∼64 per cent of the observed correlation by the residuals, whereas the black dashed contours enclose the same fraction from the relations derived from the mock data set. The comparison between these two distributions shows that the correlation we find between ΔSK and ΔSFHP is mostly driven by the strong covariance of the observables (left-hand panel of Fig. 3). The Pearson correlation coefficient derived from the mock data set is similar as the one obtained from observations ($r = 0.85$). On the other hand, the distribution of the observed relation between ΔSFMS and ΔSFHP is wider in comparison to one obtained using the mock data set (middle panel of Fig. 3). This suggests that the observed correlation between these two residuals is not entirely driven by the covariance of the observables. Finally, the distribution of the observed relation between ΔMGMS and ΔSFHP is slightly tighter than the one obtained from the mock data set (right-hand panel of Fig. 3). The Pearson correlation coefficient derived from the mock data set shows a larger anticorrelation between residuals is larger than the one obtained from observations ($r = -0.53$). The lower correlation coefficient and the smaller scatter observed between ΔMGMS and ΔSFHP – compare with those derived from the mock data – indicate that $P_{\rm h}$is a more appropriate parameter to describe $\Sigma_{\rm SFR}$ than the gas fraction. In Section 4, we further discuss the impact of individual components of the baryonic mass in the $\Sigma_{\rm SFR}$–$P_{\rm h}$ relation.

Thanks to the `edge_pydb`, we are able to estimate how stellar properties affect the $\Sigma_{\rm SFR}$–$P_{\rm h}$ relation. In the left-, middle, and right-hand panels of Fig. 4, we colour-code Fig. 2 with respect to the luminosity-weighted stellar age, stellar metallicity ([Z/H]), and the line-of-sight stellar velocity dispersion (σ_*), respectively. We find a significant anticorrelation of the stellar age and metallicity with ΔSFHP ($r = -0.25$ and -0.40, respectively). For a given $P_{\rm h}$, $\Sigma_{\rm SFR}$ decreases as the age or [Z/H] increases. This suggests that for those regions where the hydrostatic mid-plane pressure is similar, those with young/metal-poor stellar population tend to have large $\Sigma_{\rm SFR}$ in comparison to those with old/ metal-rich population. These two anticorrelations could emerge from the stellar velocity dispersion. Regions with large/low SFR for a given $P_{\rm h}$ could be dynamically cold/hot (i.e. low/high σ_*). However, in the right-hand panel of Fig. 2, when we colour-code the $\Sigma_{\rm SFR}$–$P_{\rm h}$ relation with respect to σ_*, we do not find similar patterns as those observed with the other two stellar properties in the other panels. Even more, the residuals of this relation do not seem to show a correlation with σ_* ($r = 0.01$). The spectral resolution of the CALIFA survey only allows to have a reliable estimation of σ_* at high values (i.e.∼ 60 km s^{-1}), but even for large velocity dispersions, we do not find a variation of the ΔSFHP against σ_*.

In Section 3.3, we find that the scatter of the $\Sigma_{\rm SFR}$–$P_{\rm h}$ relation apparently (anti-)correlates with the (total stellar mass) and morphology. In other words, at a fixed $P_{\rm h}$, $\Sigma_{\rm SFR}$ is higher, for lower ages and metallicities, mainly in low-mass galaxies. Since the stellar metallicity and age are features of the underlying stellar populations, both hint past properties of the ISM; however, the $\Sigma_{\rm SFR}$ is a feature of the current ISM. This could be explained by an inside-out formation scenario. It can also be the case that the observed ΔSFHPis affected by our estimation of $\Sigma_{\rm SFR}$. The IMF varies with SFR and metallicity, such that very massive stars form when the SFR is high, regardless of the stellar metallicity, but for super solar metallicities the formation of low-mass stars dominates, regardless of the SFR. The $\Sigma_{\rm SFR}$ considered in this work is computed using the Kennicutt $\Sigma_{\rm SFR}$ –Hα relation (Kennicutt 1998b). This calibration was obtained by assuming an invariant IMF for stars of solar metallicity with masses between 0.1 and 100 $M_\odot$. Therefore a secondary relation with the stellar metallicity and/or the stellar age with the $\Sigma_{\rm SFR}$–$P_{\rm h}$ relation may reflect the dependence of these stellar properties with the conversion of Hα with SFR (e.g. Jeřábková et al. 2018)..

We cannot rule out whether these secondary trends could be induced by expected relations between the components of $P_{\rm h}$and $\Sigma_{\rm SFR}$. Although we do not find strong correlations among $\Sigma_{\rm SFR}$, Σ_*, $\Sigma_{\rm mol}$ and the stellar age and metallicity, we find significant anticorrelations among the specific star formation rate (sSFR = $\Sigma_{\rm SFR}/\Sigma_*$), the star formation efficiency (SFE = $\Sigma_{\rm SFR}/\Sigma_{\rm mol}$) and the stellar age

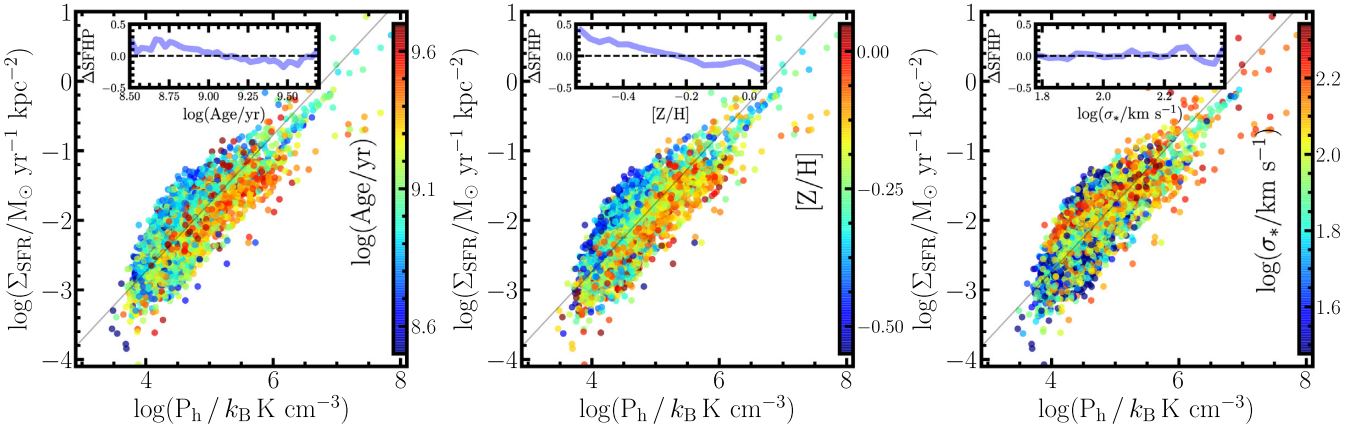

Figure 4. The impact of various stellar properties on the $\Sigma_{\rm SFR}$–$P_{\rm h}$ relation shown in Fig. 2. In the three panels, the insets show the medians of the residuals as function of the stellar parameter. The left-, middle, and right-hand panels show the $\Sigma_{\rm SFR}$–$P_{\rm h}$ relation colour-coded by the average stellar age, average stellar age ([Z/H]), and stellar velocity dispersion (σ_*), respectively. The residuals of the $\Sigma_{\rm SFR}$–$P_{\rm h}$ relation (ΔSFHP) are anticorrelated with both stellar properties; however, ΔSFHP does not seem to be strongly affected by the stellar velocity dispersion.

and metallicity, respectively. On the other hand, by construction of the $\Sigma_{\rm SFR}$–$P_{\rm h}$ relation, ΔSFHP strongly correlates with both sSFR, and SFE. These inverse relations between sSFR age and metallicity are expected, since low (high) values of sSFR (or equivalently the EW(Hα)) usually trace old/metal-rich (young/metal-poor) stellar populations (e.g. Mejía-Narváez et al. 2020).

3.3 Impact of global parameters on the $\Sigma_{\rm SFR}$–$P_{\rm h}$ relation

Having a homogeneous spatially resolved data set for a significant large sample of galaxies in the nearby Universe allow us to explore the impact of global properties on the $\Sigma_{\rm SFR}$–$P_{\rm h}$ relation. As reviewed by Sánchez (2020), most of the scaling relations derived on kpc scales in the local Universe are affected by the structural/integrated properties of their host galaxy. In particular, the total stellar mass and the morphology of a galaxy can modulate most of these relations at local scales. In Fig. 5, we colour-code the $\Sigma_{\rm SFR}$–$P_{\rm h}$ relation according to these two global observables. The top panel indicates that for regions located in low-mass galaxies $\Sigma_{\rm SFR}$ is larger in comparison to regions with similar $P_{\rm h}$ located in more massive galaxies. This trend is more evident when we plot the average residuals for each galaxy of the $\Sigma_{\rm SFR}$–$P_{\rm h}$ relation against the total stellar mass (see the inset). We find that the average ΔSFHP for each galaxy anticorrelates with the total stellar mass ($r = -0.3$). For most of low-mass galaxies ($\log(M_\odot/M_* \lesssim 10.5)$), the best fit of the $\Sigma_{\rm SFR}$–$P_{\rm h}$ relation underestimates the observed $\Sigma_{\rm SFR}$ whereas for more massive galaxies $\Sigma_{\rm SFR}$ is slightly overestimated. This is quantified by the slope of the black line in the inset (~ -0.17 dex/M_*). We note that even though this trend seems to be systematic, due to the large scatter, observations for a wider range of galaxies is required to test the robustness of the impact of the total stellar mass in shaping the local $\Sigma_{\rm SFR}$–$P_{\rm h}$ relation.

We explore whether the inclusion of the total stellar mass as a secondary parameter in the $\Sigma_{\rm SFR}$–$P_{\rm h}$ relation could induce a reduction in its scatter. If so, this would be strong evidence of the importance of the role that the potential well could have in shaping $\Sigma_{\rm SFR}$ at local scales. We measure the scatter of the relation between $\Sigma_{\rm SFR}$ and a parameter that includes the stellar mass as a secondary parameter of the form $x = \log(P_{\rm h}/k_{\rm B}\,{\rm K\,cm^{-3}}) - \alpha\ \log({\rm M_*}/10^{10}{\rm M_\odot})$ with $-1 < \alpha < 1$. We find that the value that yields the smallest scatter is $\alpha = -0.07$. The scatter of this relation is very similar to the one where the stellar mass is not included as a secondary parameter (i.e. $\sigma = 0.28$ dex). We suggest that even though the overall gravitational potential may have an impact in shaping $\Sigma_{\rm SFR}$, its impact is relatively mild in comparison to the local pressure. Further studies including larger samples of low-mass galaxies are thus required to quantify the actual impact of the potential well in this relation.

On the other hand, when we colour-code this relation according to the morphology of the host galaxies (bottom panel), regions located in late-type galaxies have a slightly large $\Sigma_{\rm SFR}$ than regions in more early-type galaxies for a similar $P_{\rm h}$. We also identify this mild trend when plotting the average residual of the $\Sigma_{\rm SFR}$–$P_{\rm h}$ relation for a given morphological type. For early-type galaxies (E-S0), the best $\Sigma_{\rm SFR}$–$P_{\rm h}$ relation overestimates $\Sigma_{\rm SFR}$ by a factor of $\sim$0.2 dex, whereas for late-type galaxies (Sc,Sd-Irr), $\Sigma_{\rm SFR}$ is underestimated by an average of $\sim$0.1 dex. Despite this apparent trend we should note that the standard deviation of the residuals for each morphological type (error bars for the white points) are consistent with no change in the residual of the $\Sigma_{\rm SFR}$–$P_{\rm h}$ relation with respect to the morphology (i.e. ΔSFHP= 0). Furthermore, the early-type galaxies where we are able to measure this relation exhibit clear signatures of interaction and/or merging (i.e. NGC 4211, NGC 4676 A, and NGC 5953). Thus, to either confirm or rule out these trends, we would require a larger sample of galaxies that includes more early-type galaxies than those currently available (see the inset in the middle panel of Fig. 1).

In Fig. 6, we plot the radial distribution of the residuals of the $\Sigma_{\rm SFR}$–$P_{\rm h}$ relation according to the position of the host galaxy in different global scaling relations presented in Fig. 1. In the top panel of Fig. 6, we plot the radial gradient of ΔSFHP dividing galaxies in three groups (low, average, and high ΔSFMS) according to their location respect the star formation main sequence (below -0.5, between -0.5 and 0.5, and above 0.5 times the standard deviation of the scatter from the black solid line in the left-hand panel of Fig. 1, respectively). Although the radial distributions are clustered around the zero residual (i.e, close to the dashed horizontal line), we find that in galaxies with higher and average SFR for their stellar mass have a flat radial gradient of their ΔSFHP. For galaxies with low ΔSFMS, ΔSFHP is negative for all radii, decreasing with radii (~ -0.07 dex/$R_{\rm eff}$). In other words, for global low star-forming galaxies, we are overestimating $\Sigma_{\rm SFR}$ when deriving it from $P_{\rm h}$, particularly at they outskirts.

Similar as above, in the middle panel of Fig. 6 we classify galaxies according to their vertical distance with respect to the black solid line

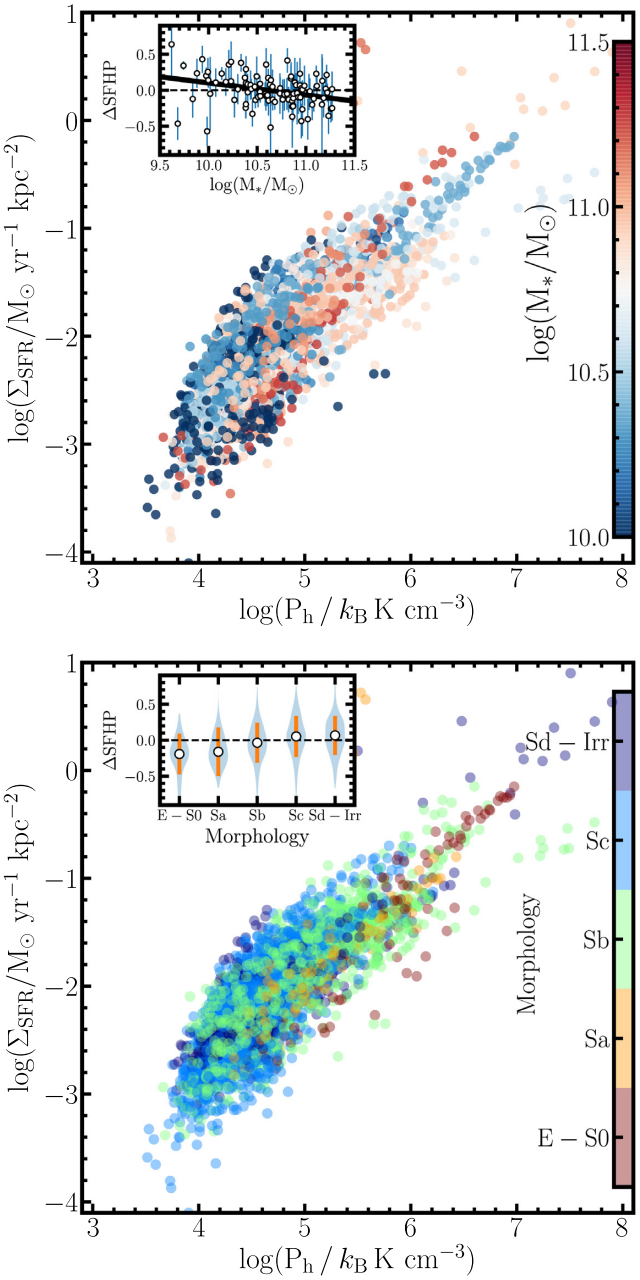

Figure 5. Top panel: the Σ_{SFR}–P_h relation colour-coded by the total stellar mass of the host galaxy. The circles in the inset show the average ΔSFHP for each galaxy against its total stellar mass while the associated error bars represent the standard deviation of ΔSFHP for each galaxy; the black solid line represents a linear fit to the averaged residuals. Bottom panel: the Σ_{SFR}–P_h relation colour-coded by the morphological type of the host galaxy. The circles in the inset show the average ΔSFHP for a given morphological type. The violin histograms in the inset represent the distribution of ΔSFHP for the different morphological types. Although there seems to be a correlation between ΔSFHP and the total stellar mass, these global properties does not seem to have a large impact in the Σ_{SFR}–P_h relation (see details in Section 3.3.).

in the middle panel of Fig. 1 (low, average, and high ΔSK). Galaxies with low and average SFR for their total gas mass have similar mildly increasing gradients (∼ 0.03 dex/R_{eff}). On the other hand, for those galaxies in the large ΔSK bin, ΔSFHP is positive for all radii (∼ 0.1 dex), even more it shows a positive gradient (∼ 0.07 dex/R_{eff}). This

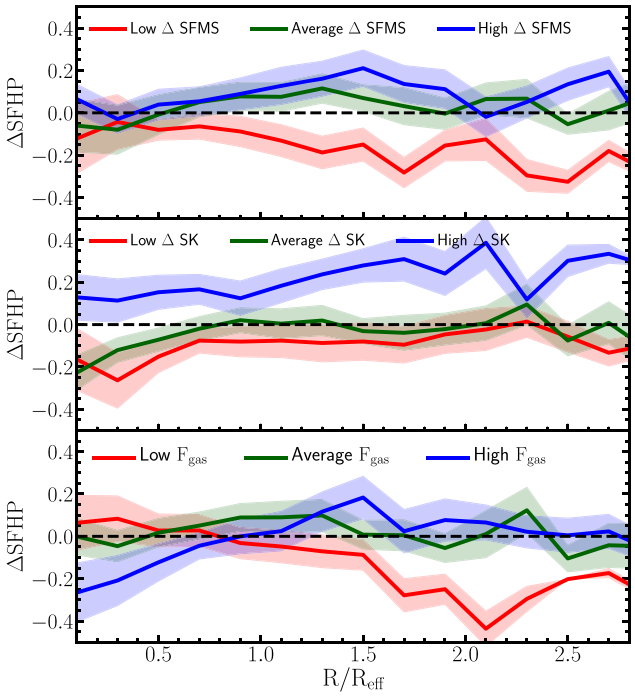

Figure 6. The radial distribution of the residuals of the Σ_{SFR}–P_h relation for three global scaling relations. For each of the global scaling relation we divi,de the sample in galaxies with low, average and high bins (red, green, and blue lines) referring to the vertical distance of the galaxy with respect to the best fit of the global scaling relation (see black solid lines in each panel of Fig. 1). In the top, middle, and bottom panels, we show the radial gradients of ΔSFHP for the star formation main sequence, the Schmidt–Kennicutt law, and the stellar–molecular mass relation, respectively. These radial trends highlight the impact of global properties in the local Σ_{SFR}–P_h relation.

suggests that for those galaxies with larger SFR, with respect to the SK-law, the Σ_{SFR} is underestimated from the local P_h, particularly at they outskirts.

Finally, we plot in the bottom panel of Fig. 6 the radial gradient of ΔSFHP for galaxies classified according to their vertical distance with respect to the black line in the right-hand panel of Fig. 1 (low, average, and high ΔF_{gas}; in other words the lack or excess of M_{mol} for a given M_*). For the average ΔF_{gas}, the radial distribution of ΔSFHP is flat and close to zero. For galaxies in the low ΔF_{gas} bin, we find a significant negative radial gradient (∼ −0.14 dex/R_{eff}), suggesting that in the outskirts of these galaxies Σ_{SFR} is overestimated by P_h. We note a dip of ΔSFHP at central regions for galaxies in the high ΔF_{gas} bin, inducing a positive gradient (∼ 0.07 dex/R_{eff}). These radial trends show the impact of global properties in the local scaling relations such as the Σ_{SFR}–P_h one.

3.4 Testing the impact of systematic in the Σ_{SFR}–P_h relation

In this section, we explore the impact of the inclination and a variable α_{CO} conversion factor on the Σ_{SFR}–P_h relation. Although all the surface densities in this study are corrected by inclination effects, to further explore the impact of galaxy projection on this relation, in Fig. 7, we plot the Σ_{SFR}–P_h relation as in Fig. 2, but colour-coding galaxies according to inclination: Regions located in low-inclination galaxies ($b/a > 0.45$) are indicated with blue crosses and regions located in high-inclination galaxies $b/a < 0.45$) are indicated with orange plus symbols. We note that on average for low inclined

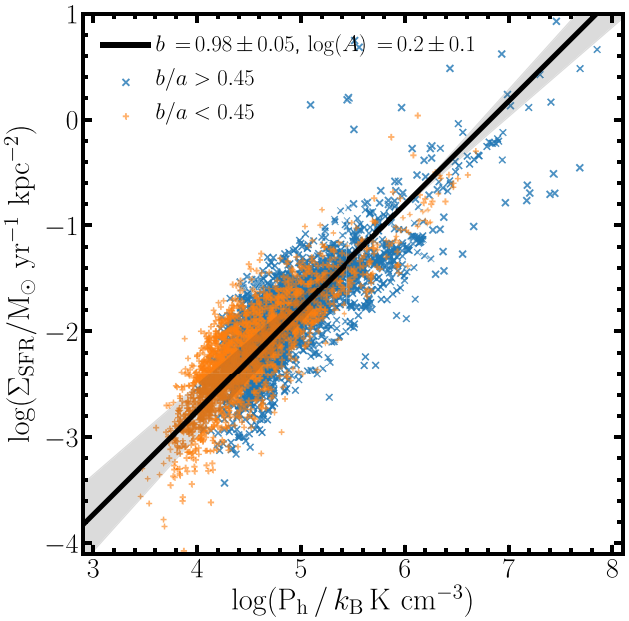

Figure 7. The Σ_{SFR}–P_h relation, with regions located in low-inclination galaxies ($b/a > 0.45$) shown with blue crosses and high-inclination ones ($b/a < 0.45$) shown as orange plus symbols. Similar to Fig. 2, the solid line representing and ODR fit to the regions in low-inclined galaxies show a good agreement with the best fit for all the sample in Fig. 2.

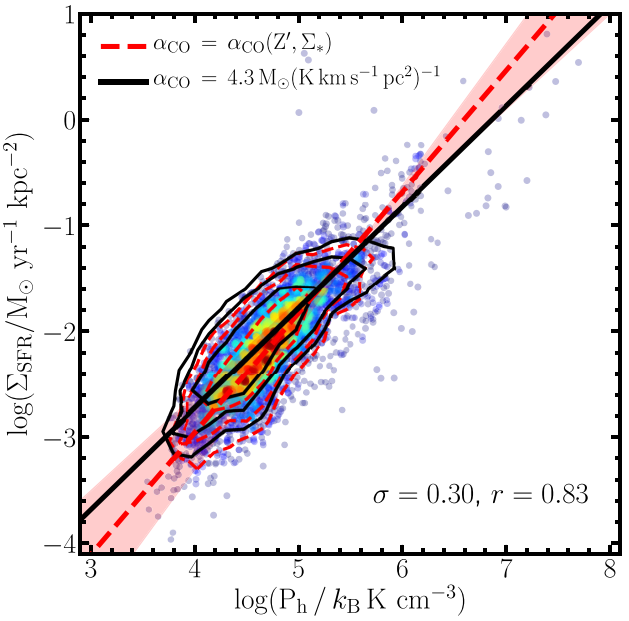

Figure 8. The red-dashed contours enclose the Σ_{SFR}–P_h relation using a variable α_{CO} conversion factor. The best ODR fit is represented by a red-dashed line, while the the red shaded area shows the uncertainty of assuming different $\Sigma_{H\,I}$ densities (see details in Section 2). The black contours and black lines are the same as those in Fig. 2. By allowing a variable α_{CO} conversion factor, the slope of the Σ_{SFR}–P_h relation is steeper than when adopting a constant factor.

galaxies P_h and Σ_{SFR} are larger compared to regions located in highly inclined galaxies. We perform a similar analysis as in Section 3.1 for the low-inclined sample. We find a smaller Pearson correlation coefficient in comparison to the entire sample ($r = 0.80$). The ODR fitting shows a similar slope by comparison to the entire sample ($b = 0.98 \pm 0.05$, $A = 0.2 \pm 0.1$). The residual of the fit is slightly larger than the one derived from the entire sample ($\sigma = 0.30$). These results show that inclination does not play a major impact in shaping the slope of the Σ_{SFR}–P_h relation.

Along this paper, we adopt a constant Milky Way value of the conversion factor between the CO luminosity and the molecular gas mass density (α_{CO}). Since α_{CO} can vary, in particular it can decrease in regions of high density and temperature where the CO excitation is higher, which are usually associated with high-pressure inner-galaxy regions (e.g. Bolatto et al. 2013; Gong et al. 2020). Here we explore how the Σ_{SFR}–P_h relation varies when including a variable α_{CO} ($\alpha_{CO}(Z, \Sigma_*)$, see equation 3). In Fig. 8, data points and red-dashed contours represent the Σ_{SFR}–P_h relation using $\alpha_{CO}(Z, \Sigma_*)$ whereas the black contours are the same as those presented in Fig. 2. We follow a similar procedure as in Section 3.1 to derive the best ODR fit to the data. We find that this fit is steeper (red-dashed line, $b = 1.14 \pm 0.07$, $A = 0.0 \pm 0.1$) in comparison to the one derived adopting a constant α_{CO} (black solid line). The slope of the best fit agrees with derivation from numerical simulations of feedback from SN explosions and photoelectric heating (Kim et al. 2013). However, the scatter of the relation is larger (and the Pearson correlation is smaller, $r = 0.83$) in comparison to the relation presented in Section 3.1.

3.5 Comparison with the literature

Using spatially resolved data from surveys including small yet significant samples of galaxies, different studies have shown the tight correlation between Σ_{SFR} and the so-called dynamical equilibrium pressure, P_{DE} (see equation 5). In this section, we compare the Σ_{SFR} – P_{DE} relation derived for our data set of spatially resolved observations of 96 star-forming galaxies from the EDGE-CALIFA survey with those relations derived in the literature.

In Fig. 9, we plot the Σ_{SFR} –P_{DE} relation for the regions sampled by the EDGE-CALIFA survey. Inwards, the contours enclose 90, 80, and 50 per cent of the distribution in this relation. The correlation coefficient of this relation is similar to the one derived for the Σ_{SFR}–P_h relation ($r = 0.85$). Despite the assumptions to derive P_{DE}, the trend observed of the Σ_{SFR}–P_{DE} relation with our data set is in good agreement with those derived in the literature for spatially resolved measurements from the HERACLES+THINGS (Leroy et al. 2008) and PHANGS surveys (Sun et al. 2020, blue x-symbols and orange crosses, respectively). Our sample covers values of Σ_{SFR} and P_{DE} similar to those derived from the PHANGS multiwavelength data set; the distribution of our estimate of pressure is slightly shifted towards lower values of Σ_{SFR} ($\sim$ 0.2 dex). Although small, this difference could be due, among others, to (i) the significant difference between the data sets (Sun et al. 2020 used the photometric data at different wavelengths such as UV, and IR, whereas here we use the IFS data set only in the optical regime) in particular this could lead to an underestimation of $\sim$0.2 dex when using the dust-corrected Hα luminosity to derive Σ_{SFR} (Hirashita, Buat & Inoue 2003, although see Catalán-Torrecilla et al. 2015), and (ii) we study a large galaxy sample (Sun et al. 2020 used a sample of 28 star-forming galaxies whereas we use a sample of 96 galaxies including massive galaxies with a wider range of morphological types; see Fig. 1). Furthermore, in Section 3.6, we find an excellent agreement with the best-fitting parameters derived by Sun et al. (2020) when selecting regions with large Hα equivalent width (EW(Hα) $\gtrsim$ 20 Å).

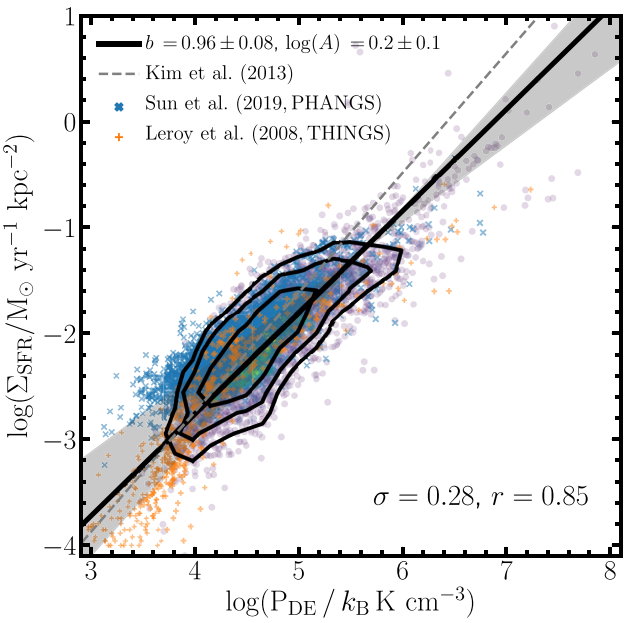

Figure 9. The Σ_{SFR}–P_{DE} relation derived for the EDGE-CALIFA galaxies (contours enclosing 90, 80, and 50 per cent of the sample) compared to spatially resolved data from previous studies. Orange plus symbols represent the data from the THINGS survey (Leroy et al. 2008). Blue crosses represent the data from the PHANGS survey (Sun et al. 2020). The solid black line represents the best fit to our data. The dashed line shows the prediction from hydrodynamic simulations (Kim et al. 2013). Despite the differences in observables and samples size, the Σ_{SFR}–P_{DE} relation for the EDGE-CALIFA sample is in agreement with previous estimates from smaller samples of galaxies.

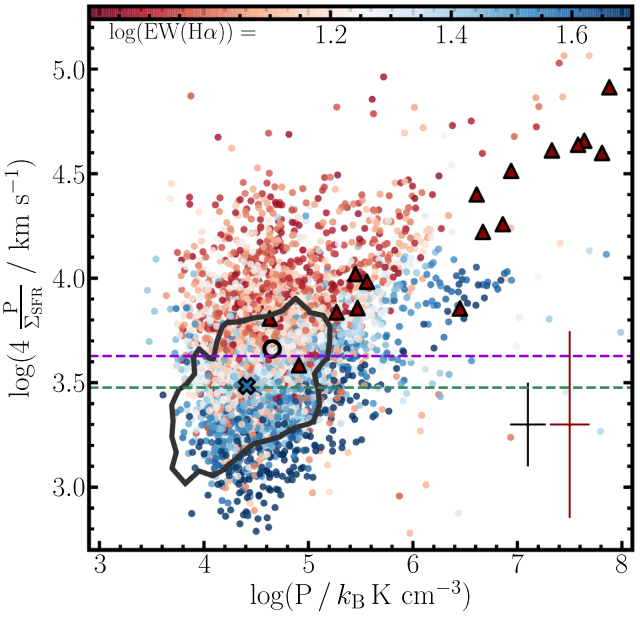

Figure 10. The 4 P/Σ_{SFR} ratio against P. The points are colour-coded by the EW(Hα) representing the 4 P_h/Σ_{SFR} versus P_h relation for the regions sampled in this study. The grey contour encloses 80 per cent of the 4 P_{DE}/Σ_{SFR} versus P_{DE} relation derived for regions included in 28 star-forming PHANGS galaxies (Sun et al. 2020). The empty circle and large blue cross represent the locations of the median ratio and pressure for the previous distributions, respectively. The triangles represent the integrated measurements from highly turbulent galaxies included in the DYNAMO survey (Fisher et al. 2019). The black and red error bars represent the typical uncertainty for our data set and the DYNAMO data, respectively. The dashed green line represents the typical value adopted as the feedback-driven momentum injection per unit mass of stars formed (3000 km s^{-1}; Ostriker & Shetty 2011; Fisher et al. 2019). The dashed violet line represents the sum of the aforementioned momentum injection with the one derived from the stellar winds and radiation pressure produced by a typical starburst population ($\sim$ 4200 km s^{-1}; Heckman et al. 2015; Heckman & Thompson 2017). Active star-forming regions are in agreement with both the feedback-driven momentum injection and the median values from the literature.

The HERACLES-THINGS survey, on the other hand, traces the Σ_{SFR}–P_{DE} relation mainly for galaxies with lower stellar mass than our sample (see Fig. 1). For a fraction of radial bins (those with similar values of P_{DE}), the Σ_{SFR}–P_{DE} relation derived from the this survey is in agreement with those derived in this study. However, there is a significant fraction of HERACLES-THINGS radial bins that have smaller values of P_{DE} in comparison to those estimated from the EDGE-CALIFA or PHANGS surveys. Those radial bins exhibit a low values of Σ_{SFR} in comparison to those expected from the previous surveys. It can be the case that for regions with $P_{DE}/k_B \lesssim 10^4$ K cm^{-3}, the Σ_{SFR} does not follows a power-law relation (or with a different index) as the one described for the bulk of our observations.

Following the same procedure as in Section 3.1, we derive the best fit for the Σ_{SFR}–P_{DE} relation. The best relation from an ODR fit is similar – within uncertainties – to the one derived in Section 3.1 for the Σ_{SFR}–P_h relation ($b = 0.96 \pm 0.08$, $\log(A) = 0.2 \pm 0.1$). The scatter of this relation is similar to the one derived for the Σ_{SFR}–P_h relation ($\sigma = 0.28$). The slope of this fit is in agreement with estimations using CO stacked spectra from the EDGE-CALIFA survey (Villanueva et al. in preparation). On the other hand, an OLS fitting of this relation is in good agreement with the best fit derived from the PHANGS data set ($b = 0.84 \pm 0.04$, $\log(A) = 0.4 \pm 0.1$). The trend observed for our derivation of the Σ_{SFR}–P_h relation agrees with the prediction from a hydrodynamic simulation ($b = 1.13$, and $\log(A) = 0.26$; Kim et al. 2013). As mentioned by Sun et al. (2020) using the PHANGS data, our observations also show a shallower slope in comparison to the value expected from the simulation, in particular at large values of P_{DE}. This difference in slope could reflect systematic effects of the ISM at different locations of the galaxies or the change of the properties for massive galaxies. In Section 3.6, we further explore these possibilities. In summary, despite the samples sizes and their differences in their measurement, our estimation of the Σ_{SFR}–P_{DE} relation is in good agreement with those presented previously in the literature.

3.6 The P_h/Σ_{SFR} ratio

From star formation theory, the ratio between the pressure (P) and the Σ_{SFR} is proportional to the momentum injection per unit mass mostly from supernovae to the ISM, p_*/m_* (e.g. Ostriker & Shetty 2011; Shetty & Ostriker 2012; Faucher-Giguère et al. 2013; Kim et al. 2017). These studies usually adopt or derive a constant value for this ratio that ranges between $\sim 10^3$ and 10^4 km s^{-1}, depending on the adopted conditions for the ISM, the clustering of the supernovae and losses due to interphase mixing (e.g. Iffrig & Hennebelle 2015; Kim & Ostriker 2015; Martizzi, Faucher-Giguère & Quataert 2015; Walch & Naab 2015; Kim et al. 2017; El-Badry et al. 2019; Gentry et al. 2019). In Fig. 10 we compare the 4 P/Σ_{SFR} ratio against P, usually this ratio is expressed in units of km s^{-1}. The factor of 4 comes from assuming that a spherical injection of the momentum

flux is centred in the disc mid-plane and that this momentum is converted directly into turbulent pressure (Ostriker & Shetty 2011); this factor has been directly verified in numerical simulations of disc galaxies (see fig. 15 of Kim et al. 2013). In this figure we plot the $4\,P_{\rm h}/\Sigma_{\rm SFR}$ –$P_{\rm h}$ distribution adopting a constant CO conversion factor. Our sample covers a large dynamical range of the $4\,P_{\rm h}/\Sigma_{\rm SFR}$ ratio (from 5.1×10^2 to 1.6×10^5 km s^{-1}). The median of this ratio is 4.3×10^4 km s^{-1} (see empty circle in Fig. 10). We also derive this ratio assuming a variable CO conversion factor (see Equation 3). We find larger values for the $4\,P_{\rm h}/\Sigma_{\rm SFR}$ ratio when adopting a variable CO conversion factor with a median of $\sim$6.4 $\times$ 10^4 km s^{-1}. On the other hand, we colour-coded each region according to their H$\,\alpha$ equivalent width, EW(H$\,\alpha$). Since this parameter captures the contrast between the adjacent stellar continuum and the H$\,\alpha$ emission lines, it has been considered as a tracer of the star formation activity (e.g. Lacerda et al. 2018; Sánchez 2020). For a given $P_{\rm h}$, we find a clear trend: Regions with large EW(H$\,\alpha$) have lower values of the $4\,P_{\rm h}/\Sigma_{\rm SFR}$ ratio. This is particularly evident for regions with the median $P_{\rm h}(\sim 10^{4.4}$ K cm$^{-3})$.

Using the data from Sun et al. (2020), we derive the $4\,P_{\rm DE}/\Sigma_{\rm SFR}$ – $P_{\rm DE}$ distribution from the PHANGS survey (grey contour enclosing 80 per cent of their sample). The average $4\,P_{\rm DE}/\Sigma_{\rm SFR}$ is smaller than those derived from our regions using $P_{\rm h}(\sim 3.0 \times 10^3$ km s^{-1}; see the thick large cross in Fig. 10). As we mention in Section 3.5, these differences can be expected due to the equations used to estimate $P_{\rm DE}$ and $P_{\rm h}$, the observables used to derive $\Sigma_{\rm SFR}$, and the observed samples of galaxies. Despite these differences, the distribution agrees with our sample, in particular with those regions that show large star formation activity. In fact, the observed trend for the blue regions (i.e. regions with high star formation activity, EW(H$\,\alpha$) $\gtrsim$ 20 Å), agrees with the distribution of the $4\,P_{\rm DE}/\Sigma_{\rm SFR}$ to $P_{\rm DE}$ ratio from the PHANGS survey. The $P/\Sigma_{\rm SFR}$ ratio increases with P. A similar trend is also observed for integrated properties of highly turbulent galaxies included in the DYNAMO survey (Fisher et al. 2019, although a shift of $\sim$−0.2 dex in both axis can be expected due to improved estimations of their $P_{\rm h}$; Girard et al., submitted, the observed trend holds). The black and red error bars represent the typical uncertainties for our data set and the DYNAMO data, respectively. The uncertainties of both data sets increase as $4\,P_{\rm DE}/\Sigma_{\rm SFR}$ increases, suggesting that regions with very large ratios could be considered as upper limits.

Following Kim & Ostriker (2015), we adopt a fiducial value of $\sim$3000 km s^{-1} as the value of the p_*/m_* expected from supernovae (dashed green horizontal line). Based on the stellar models from STARBURST99 (Leitherer et al. 2014), we add to this estimation the momentum injection to the ISM produced by a combination of stellar winds and radiation pressure ($\sim$ 1200 km s^{-1}, dashed violet horizontal line; Heckman & Thompson 2017). This value should be considered as an upper limit from the stellar models since the momentum flux due to stellar winds for a typical starburst population is smaller and can vary depending on the assumptions of the models ($\sim$ 400–700 km s^{-1}; e.g. Ostriker & Shetty 2011; Heckman et al. 2015). On the one hand, we find that a significant fraction of regions in our sample ($\sim$ 50 per cent) have a $4\,P_{\rm h}/\Sigma_{\rm SFR}$ ratio larger than the expected values of momentum injection from models and simulations of star formation. On the other hand, we find that, when we only consider active star-forming regions (EW(H$\,\alpha$) $\gtrsim$ 20 Å), the median ratio is consistent with the momentum injection due to SNe explosions ($\sim 3.3 \times 10^3$ km s^{-1}). We note that the median $4\,P_{\rm DE}/\Sigma_{\rm SFR}$ from PHANGS is in good agreement with the expectation that momentum injection to the ISM is most likely driven by supernovae.

We recall that one of our selection criteria to ensure that we are only considering star-forming regions in our sample is that their EW(H$\,\alpha$) > 6 Å (see Section 2). However, we find that for those regions considered as active star-forming (i.e. EW(H$\,\alpha$) $\gtrsim$ 20 Å), the $4\,P_{\rm h}/\Sigma_{\rm SFR}$ ratio could indeed be represented by the momentum injection per mass unit expected from SNe, stellar winds, and radiation pressure. The trend observed between $4\,P_{\rm h}/\Sigma_{\rm SFR}$ and $P_{\rm h}$ is similar as those derived using (un-)resolved measurements in other star-forming galaxies (Fisher et al. 2019; Sun et al. 2020). Furthermore, when selecting regions with EW(H$\,\alpha$) $\gtrsim$ 20 Å, we find a tighter $\Sigma_{\rm SFR}$–$P_{\rm h}$ relation (σ= 0.22 dex) with a strong correlation coefficient (r = 0.90) and best-fitting ODR parameters very similar as those derived for the PHANGS survey ($b = 0.88 \pm 0.05$, log (A) $= 0.5 \pm 0.1$).

There could be different reasons that explain why we find a significant fraction of star-forming regions with low EW(H$\,\alpha$) with large $4\,P_{\rm h}/\Sigma_{\rm SFR}$ ratios. We recall that we are convolving the optical maps – including the H$\,\alpha$ map – to have a common spatial resolution as the CO maps ($\sim$ 7 arcsec). This may induce a dilution of both the $\Sigma_{\rm SFR}$ and the EW(H$\,\alpha$) for a given value of $P_{\rm h}$. Thus, for a given sampled area with a low value of EW(H$\,\alpha$), we may be including some active star-forming regions and some others with no significant star formation (regions with EW(H$\,\alpha$) < 6 Å; e.g. diffuse ionized gas). On the other hand, in comparison to previous studies exploring the $\Sigma_{\rm SFR}$–P relation at (sub)kpc scales (e.g. Leroy et al. 2008; Sun et al. 2020), our sample covers a large number of galaxies. This implies that we are probing different regimes of star formation, including those where star formation is not as intense as those probed previously. This maybe the case for the massive galaxies that we sampled (see Section 3.3). It could also be the case that our measurements (i.e. equation 1) overestimates the pressure in those regions with EW(H$\,\alpha$) < 20 Å. This is certainly the case for regions located in structures of galaxies others than the disc like a bulge or a bar. We find that although central regions (i.e. those with $R/R_{\rm eff}$ < 0.5) own the highest pressures ($\sim 10^{5.5}$ K cm^{-3}), they exhibit a wide range of $4\,P_{\rm h}/\Sigma_{\rm SFR}$ ratios and EW(H$\,\alpha$); even more, they represent only $\sim$17 per cent of our sample. Thus, those regions with large $4\,P_{\rm h}/\Sigma_{\rm SFR}$ ratios and low EW(H$\,\alpha$) are not usually located in central regions of galaxies where the bulge dominates. Furthermore, in Section 4, we show that barred galaxies have a similar distribution of the $4\,P_{\rm h}/\Sigma_{\rm SFR}$ ratio in comparison to disc galaxies. From the observational data, we suggest that for those regions with small EW(H$\,\alpha$) – but still considered star-forming regions, 6 < EW(H$\,\alpha$) < 20 Å – the feedback provided from $\Sigma_{\rm SFR}$ may not be sufficient to balance the pressure estimated from the stellar and gas mass densities leading to the observed large $4\,P_{\rm h}/\Sigma_{\rm SFR}$ ratios. Finally, we note that this analysis assumes that the pressure produced by star formation feedback is mainly due to the specific momentum injected by SNe, $p_*/(4m_*)$. However, Ostriker et al. (2010) argued that in regions of low shielding, the thermal pressure and magnetic pressure (both driven by feedback) are expected to be comparable to the turbulent pressure, and this has been verified in solar neighborhood simulations by Kim & Ostriker (2015, 2017). Other potential sources of pressure associated with star formation, including cosmic rays and radiation, could also contribute to increasing the ratio of pressure to star formation (see e.g. Ostriker & Shetty 2011; Diesing & Caprioli 2018). It could be the case that the observed $P_{\rm h}/\Sigma_{\rm SFR}$ ratios for regions with low EW(H$\,\alpha$) are affected by more sources of feedback other than SNe.

4 DISCUSSION

In this study, we describe and explore the $\Sigma_{\rm SFR}$–$P_{\rm h}$ relation at kpc scales for star-forming regions located in a sample of 96 galaxies included in the EDGE-CALIFA survey. In Section 3.1, we find that this is a tight relation (i.e. with a small scatter, ∼0.2 dex), with a significant correlation coefficient ($r = 0.85$; see Fig. 2). This highlights the impact of $P_{\rm h}$ in shaping $\Sigma_{\rm SFR}$ at local scales suggesting a scenario in which star formation activity is self-regulated. As we mention in Section 1, averaged on scales of kpc and Myr, the feedback from SNe and stellar winds from massive stars counteracts the pressure from the gravity produced by the baryonic mass content (e.g. Thompson et al. 2005; Ostriker & Shetty 2011; Faucher-Giguère et al. 2013). In this section, we discuss the implications of the slope we find for the $\Sigma_{\rm SFR}$–$P_{\rm h}$ relation (Section 4.1). We also discuss possible explanations for the correlations (or lack thereof) we observe between the residuals of other star-forming scaling relations and those derived from this relation as well as their anticorrelation with stellar properties (Section 4.2). Finally, we discuss the impact of global properties on the $\Sigma_{\rm SFR}$–$P_{\rm h}$ relation (Section 4.3).

4.1 The slope of the $\Sigma_{\rm SFR}$–$P_{\rm h}$ relation

Despite the uncertainty in deriving the best $\Sigma_{\rm SFR}$–$P_{\rm h}$ relation due to the lack of information regarding the atomic gas distribution for our sampled galaxies, the range of slopes that best describe this relation are slightly sublinear. In Section 3.1, we derive the $\Sigma_{\rm SFR}$–$P_{\rm h}$ relation assuming an expected range of $\Sigma_{\rm HI}$ densities. The average value of these slopes after 1000 realizations with different $\Sigma_{\rm HI}$ densities is $b \sim 0.9$. As we find in Section 3.4, this slope depends on different parameters including the CO conversion factor.

From a theoretical point of view, there are analytical models and numerical simulations of star formation in disc galaxies suggesting that star formation is a self-regulated process. In this scenario, the hydrostatic pressure is balanced by different feedback sources such as turbulent (from stellar winds, supernovae), thermal, magnetic and radiative pressure produced from young stellar objects (e.g. Ostriker et al. 2010; Ostriker & Shetty 2011; Shetty & Ostriker 2012; Kim et al. 2013; Krumholz et al. 2018). The $\Sigma_{\rm SFR}$–$P_{\rm h}$ relation predicted from these studies is given by $\Sigma_{\rm SFR} = P/\eta_{\rm tot}$, where $\eta_{\rm tot}$ is the total feedback yield associated with young stars, and the contribution from turbulent pressure, $\eta_{\rm turb} = p_*/(4m_*)$ is typically the largest single term (see Section 3.6). Allowing for a dependence of η on environment, this yields $\Sigma_{\rm SFR} \propto P^b$, where the power-law index, b, is either unity (for analyical models; e.g. Ostriker & Shetty 2011) or slightly supralinear (∼ 1.13, for numerical simulations; Kim et al. 2013). Within the uncertainties, we consider that the $\Sigma_{\rm SFR}$–$P_{\rm h}$ relation derived from EDGE-CALIFA galaxies is in agreement with the predicted linear slope from theory of star formation. In Sections 3.1 and 3.5, we find that for both estimates of the pressure ($P_{\rm h}$ and $P_{\rm DE}$), a linear relation describe the bulk of our data set. However, we observe differences in the slopes depending on the fitting technique we consider. The slopes derived from the OLS fit ($b \sim 0.84$) are flatter than those derived using a ODR fit ($b \sim 0.95$) for both the $\Sigma_{\rm SFR}$–$P_{\rm h}$ and $\Sigma_{\rm SFR}$–$P_{\rm DE}$ relations.

As we mention in Section 3.5, similar slopes have been observed using different samples and data sets. The slope derived from the spatially resolved data set from the PHANGS survey using an OLS bisector method the fit is $b \sim 0.84$ (Sun et al. 2020), while from unresolved measurements from DYNAMO galaxies, the slope is also sublinear (b ∼0.76; Fisher et al. 2019). Sun et al. (2020) suggested that one possible reason for which they found a sublinear slope in the $\Sigma_{\rm SFR}$–$P_{\rm DE}$ relation could be the fact that they sampled galaxies/regions for typical star-forming galaxies where the most extreme cases of star formation have not yet been tested. Thus, these author suggested that in order to fully explore the slope of the $\Sigma_{\rm SFR}$–$P_{\rm DE}$ relation, extreme star-forming regions (or 'starburst' regime) such as the central regions of ultraluminous infrared galaxies (ULIRGs) should be also included in the previous analysis.

From their results using unresolved measurements, Fisher et al. (2019) suggested different scenarios that could explain the sublinear slope they found in their sample of highly turbulent galaxies. They consider that the $\Sigma_{\rm SFR}$–$P_{\rm h}$ relation can be truly sublinear, the p_*/m_* ratio increases with the pressure, or/and there are other mechanisms that sustain the pressure in disc galaxies. Numerical simulation of star formation regulated by feedback have shown a qualitatively sublinear relation between the $\Sigma_{\rm SFR}$ and the pressure (Benincasa et al. 2016). These simulations suggest that the feedback has a non-linear impact in the scale height of the galaxy. In turn, this affects the second term of equation (1), specifically the $\sigma_{\rm mol}/\sigma_{\rm stars,\,z}$ ratio. To estimate $P_{\rm h}$, we have adopted – as most of the observational studies in this regard – a constant stellar scale height across the galaxy disc, which, in turn, is proportional to their stellar scale length (see Section 2). Although the scale height may vary for different position of the disc, we consider that this does not strongly affect the estimation of $P_{\rm h}$ and thus the slope $\Sigma_{\rm SFR}$–$P_{\rm h}$ relation. In Appendix A, we show that adopting different estimations of the stellar length yield very similar values of the $\sigma_{\rm mol}/\sigma_{\rm stars,\,z}$ ratio. Furthermore, Sun et al. (2020) have found that the stellar scale height and length are tightly correlated for their sample of star-forming galaxies, supporting that indeed the scale height can be considered as constant across the galaxy.

In Section 3.6, we show that the median value of the $4\,P_{\rm h}/\Sigma_{\rm SFR}$ ratio (an observational proxy for p_*/m_*) is larger than the fiducial value expected from the momentum flux injection from SNe (see Fig. 10). Nevertheless, for most of the regions with high star formation activity (i.e. EW(Hα) > 20 Å), the $4\,P_{\rm h}/\Sigma_{\rm SFR}$ ratio is in agreement with a momentum injection per unit mass of star formed produced by SNe. For those active star-forming regions, we also find that this ratio increases with $P_{\rm h}$. This trend is also suggested by the $4\,P_{\rm DE}/\Sigma_{\rm SFR}$ –$P_{\rm DE}$ reported by the PHANGS survey (grey contour in Fig. 10; Sun et al. 2020) as well as the unresolved measurement from DYNAMO galaxies (red triangles with error bars in Fig. 10; Fisher et al. 2019). In fact, using those unresolved measurement Fisher et al. (2019) suggested that this ratio is not constant across the discs of star-forming galaxies increasing with pressure, leading to the sublinearity found in the $\Sigma_{\rm SFR}$–$P_{\rm DE}$ relation. For our sample, we find this is the case, in particular, for regions with large EW(Hα). This suggests that for those regions, the pressure can be inducing a variation of p_*/m_*, which, in turn, may play a significant role in shaping the $\Sigma_{\rm SFR}$–$P_{\rm DE}$ relation. Our results from Section 3.6 also suggest that there could be other processes that can induce departures from the $4\,P_{\rm h}/\Sigma_{\rm SFR}$ ratio expected from the momentum injection from SNe, in particular for regions with low star formation. Those physical processes that could include magnetic, and/or thermal pressure or cosmic rays may be very relevant to balance the mid-plane hydrostatic pressure in those low star formation regions.

Different studies have suggested the relevance of other processes than supernovae explosions that can maintain the pressure support in disc galaxies. From their measurements of the relation between the turbulent pressure and $\Sigma_{\rm SFR}$, Sun et al. (2020) suggested that radial inflows induced by structures such as bars or bulges could be another source of turbulent pressure. On the other hand, models that include momentum flux injection to the ISM from other sources, such as radiation pressure, photoionization, and winds, can contribute to the

pressure (e.g. Hopkins, Quataert & Murray 2011; Murray, Ménard & Thompson 2011; Hopkins et al. 2014), although the ray-tracing simulations of Kim, Kim & Ostriker 2018 (see their fig. 12) show that the specific momentum injection from radiation is small compared to that from SNe, and simulations from Lancaster et al. (2021, submitted) found that wind momentum contributions are also much smaller than from SNe. In the same direction, recent models of star formation suggest that radial transport and feedback from supernovae can have similar impact in regulating star formation in disc galaxies (Krumholz et al. 2018). In any case, these models/simulations are still needed to explain the observed relation between $\Sigma_{\rm SFR}$ and the pressure at kpc scales for the sample of galaxies in this study.

Finally, we note that the slope of the $\Sigma_{\rm SFR}$–$P_{\rm h}$ relation can vary depending on the assumption to derive the physical quantities. In Section 3.4, we show that the slope of this relation can vary when assuming a variable CO conversion factor ($b \sim 1.15$). Furthermore, in Section 3.6, we find that the observed correlation between 4 $P_{\rm h}/\Sigma_{\rm SFR}$ and $P_{\rm h}$is reduced once we consider a variable CO conversion factor. We suggest that a larger sample of galaxies (covering a wider range of chemical abundances) is required to further understand the impact of the assumption in the derived quantities.

4.2 The impact of $P_{\rm h}$ on other star-forming relations

In Section 3.2, we find strong correlations between the residuals of the $\Sigma_{\rm SFR}$–$P_{\rm h}$ relation, ΔSFHP, and those derived for the rSFMS (ΔSFMS; see equation 8) and those from the rSK relation (ΔSK; see equation 7). In contrast, we do not find a strong correlation between the residuals of the rMGMSe (ΔMGMS) and ΔSFHP(see Fig. 3). The main goal of this comparison is to quantify whether individual components of the baryonic mass density are driving star formation at kpc scales in the EDGE-CALIFA galaxies. Ellison et al. (2020) found a significant correlation between the residuals of the resolved star-forming scaling relation (ΔSK and ΔSFMS) and a secondary correlation with the residuals of the rMGMS (ΔMGMS) and the ΔSFMS. From their results, they suggested that star formation at kpc scales is primarily regulated by the amount of molecular gas, $\Sigma_{\rm mol}$, with a secondary role for the star formation efficiency, SFE. In the top panels of Fig. 11, we illustrate these results. The left-hand panel shows the rSFMS colour-coded by $\Sigma_{\rm mol}$. The right-hand panel shows the rSK relation colour-coded by Σ_{*}. In both panels, the effect that $\Sigma_{\rm mol}$ and Σ_{*} has on each of these relations is clear. For a given value of Σ_{*} ($\Sigma_{\rm gas}$), $\Sigma_{\rm SFR}$ changes with respect to $\Sigma_{\rm gas}$ (Σ_{*}). Therefore, it is expected to find significant correlation between the residuals of these relations.

In the bottom panels of Fig. 11, we colour-code the regions in the $\Sigma_{\rm SFR}$–$P_{\rm h}$ plane according to their gas and stellar mass densities (left- and right-hand panels, respectively). Contrary to the relations in the top panels, these plots show that for a given range of pressures there is no significant change in the values of either $\Sigma_{\rm gas}$ or Σ_{*}. By construction, $P_{\rm h}$ is a combination of both Σ_{*} and $\Sigma_{\rm gas}$ (see equation 1). Thus, by including these two terms, the variations in ΔSFHP are going to scale in a similar way as those observed in the rSFMS or the rSK relation. The vertical distribution of both $\Sigma_{\rm gas}$ and Σ_{*} in the $\Sigma_{\rm SFR}$–$P_{\rm h}$ plane could also explain the lack of relation between ΔSFHP and ΔMGMS. Previous studies suggested that the $\Sigma_{\rm gas}$ Σ_{*}product (or their linear combination in logarithmic scales) better describes $\Sigma_{\rm SFR}$ than each of them (the so-called extended Schmidt–Kennicutt relation, e.g. Shi et al. 2011, 2018). Although the expected correlation from these studies has not yet been corroborated using IFS data sets (Lin et al. 2019; Barrera-Ballesteros et al. 2021), the fact that we find stronger correlation coefficients for the $\Sigma_{\rm SFR}$–$P_{\rm h}$ relation (see Section 3.1), small scatter in comparison to the rSFMS and the rSK (Sánchez et al. 2021), and the relations presented in Section 3.2 suggests that the primary driver for the star formation at kpc scales rather than the individual components of the baryonic mass density is the hydrostatic pressure, $P_{\rm h}$.

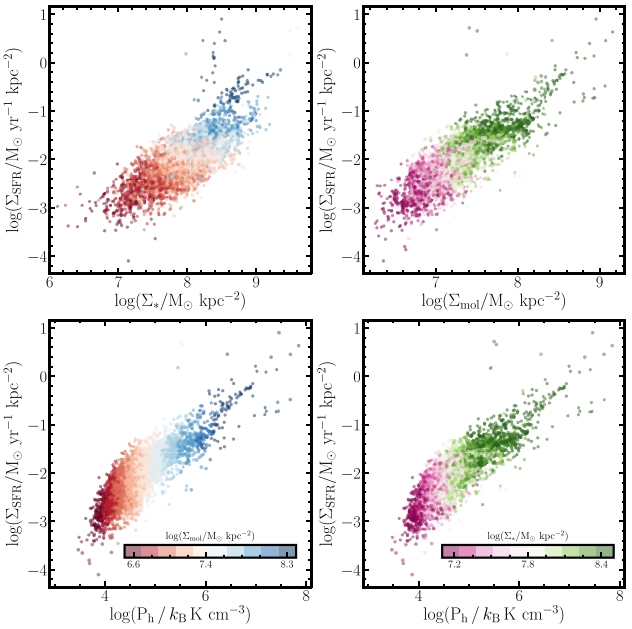

Figure 11. Comparison between the rSFMS (top left-hand panel), the rSK law (top right-hand panel), and the $\Sigma_{\rm SFR}$–$P_{\rm h}$ relation (bottom panels). The relations in the left-hand panels are colour-coded by the molecular gas mass surface density, $\Sigma_{\rm mol}$, whereas the right-hand panels are colour-coded by the stellar mass surface density. In contrast to the single-variable star-forming scaling relations, the colour-coding illustrate the minimal impact that either $\Sigma_{\rm gas}$ or Σ_{*}has in shaping $\Sigma_{\rm SFR}$ once $P_{\rm h}$ is considered as the independent variable.

4.3 The impact of global properties on the $\Sigma_{\rm SFR}$ -$P_{\rm h}$ relation

In Section 3.3, we find that the residuals of the $\Sigma_{\rm SFR}$–$P_{\rm h}$ relation apparently correlate with the total stellar mass (see the top panel of Fig. 5). However, we did not find a strong reduction of the scatter of this relation when we include the total stellar mass as a secondary parameter. We consider that even though for a given $P_{\rm h}$those regions with high/low $\Sigma_{\rm SFR}$ tend to be in low-mass/massive galaxies, the pressure is the main parameter that modulates $\Sigma_{\rm SFR}$ at local scales.

We also explore how the $\Sigma_{\rm SFR}$–$P_{\rm h}$ relation is affected by the morphology of the host galaxy (see the bottom panel of Fig. 5). Our analysis shows a mild variation of the residual for different morphological types. We indicate in Section 2 that most of the targets in our sample are late type galaxies and very few are early-type (see the inset in the middle panel of Fig. 1). For those few early-type galaxies, we note that the best $\Sigma_{\rm SFR}$–$P_{\rm h}$ slightly overestimated $\Sigma_{\rm SFR}$. This may be a hint of the so-called morphological quenching where $\Sigma_{\rm SFR}$ is halted due to the presence of a bulge rather than the absence of molecular gas (e.g. Martig et al. 2009; Colombo et al. 2018). In order to further explore this very interesting possibility, we require a larger sample of galaxies with significant bulge fraction than the one provided in this study. On the other hand, we remind ourselves that the estimation of $P_{\rm h}$ has been derived under the assumption of a thin disc (see equation 1), therefore it may be not

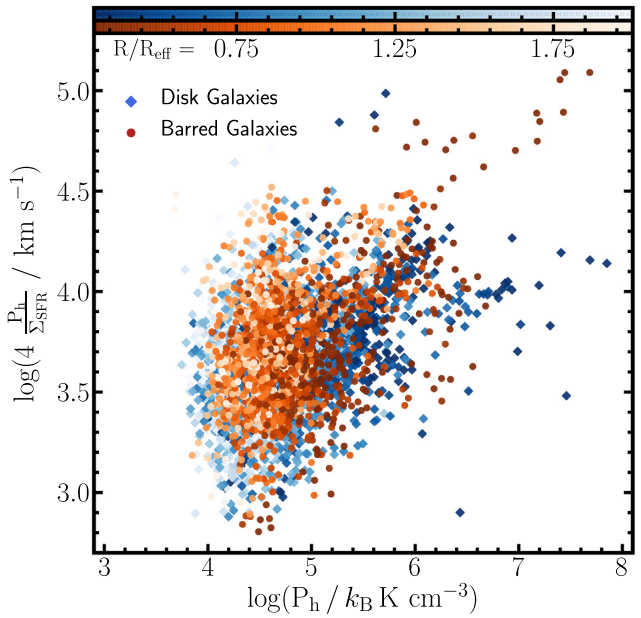

Figure 12. Similar to Fig. 10. The colour of the data points varies according to the galactocentric distance, and darker data points indicate regions located closer to centre of each galaxy. *Orange-like* circles represent the regions located in barred galaxies, whereas *bluish* diamonds represent the regions located in disc galaxies. Central regions located in barred galaxies tend to have larger $4\,P_h/\Sigma_{SFR}$ ratios.

valid for a bulge-dominated galaxies, which, in turn, may lead to this overestimation.

In Section 4.1, we suggest that alternative venues that could sustain the pressure other than feedback from supernovae in disc galaxies could be the presence of a bulge or a bar (e.g. Sun et al. 2020). A significant fraction of our sample includes barred galaxies ($\sim$ 44 per cent, 45/101) allowing us to test statistically the impact of bars in the estimation of the Σ_{SFR}–P_h relation. In Fig. 12, we compare the regions located in bars and disc galaxies in the $4\,P_h/\Sigma_{SFR}$ – P_h plane. Data points are coloured by their galactocentric distance with darker points representing regions closer to the centre. It is expected that central regions are those with the highest pressures. According to Sun et al. (2020), we would expect that those regions with large values of the $4\,P_h/\Sigma_{SFR}$ ratio are located preferentially in barred galaxies. Fig. 12 shows that regions with large values of $4\,P_h/\Sigma_{SFR}$ ratio are located in both barred and disc galaxies. However, there are more regions with $4\,P_h/\Sigma_{SFR} \gtrsim 10^{4.5}$ km s^{-1} in barred galaxies than in disc galaxies (20 versus 6). Regions with the highest pressures and the largest $4\,P_h/\Sigma_{SFR}$ ratios are located in barred galaxies. Also, the median value of the $4\,P_h/\Sigma_{SFR}$ ratio is slightly larger for regions located in barred galaxies than for those located in disc galaxies ($\sim$ 5015 versus 4500 km s^{-1}). Overall, we suggest that bars have a rather mild impact in setting the pressure at kpc scales. Detailed numerical simulations exploring the role of the radial motions as source of pressure are required to quantify these trends.

5 CONCLUSIONS

The spatially resolved data set from the EDGE-CALIFA survey (Bolatto et al. 2017) allows us to estimate the relation between the star formation rate density, Σ_{SFR}, and the hydrostatic mid-plane pressure, P_h, for a sample of 4260 star-forming regions located in 96 galaxies of the nearby Universe. This sample covers a significant range of properties, which is essential to test the impact of global observables on this spatially resolved scaling relation. The main results of this study are as follows:

(i) We find that Σ_{SFR} strongly correlates with P_h (Pearson correlation coefficient, $r = 0.84$). This correlation is tight (scatter $\sim$0.2 dex). The bulk of this relation is in agreement with a linear relation, suggesting that star formation is an autoregulated process.

(ii) From the $4\,P_h/\Sigma_{SFR}$ ratios, we suggest that one of the main source of momentum flux injection to the ISM comes from supernovae explosions, in particular for those regions considered as actively star-forming ones (i.e. EW(Hα) $>$ 20 Å). For those regions with EW(Hα) $<$ 20 Å, we suggest that either it is required to invoke other sources of pressure such as magnetic, and/or thermal pressure or cosmic rays or that the measured Σ_{SFR} in those regions from the Hα emission line may be polluted with emission not corresponding to pure star-forming regions (e.g. diffuse ionized gas).

(iii) The strong correlation coefficient of the Σ_{SFR}–P_h relation in comparison to other star-forming scaling relations (such as the rSFMS and the rSK), the fact that its scatter is very similar to the scatter of those scaling relations, and that its residuals do not correlate with the residuals of the molecular gas main sequence, indicate that P_h is probably the main driver of Σ_{SFR} at kpc scales rather than individual components of the baryonic mass.

(iv) Total stellar mass may play a role in shaping the local Σ_{SFR}. For a given P_h, Σ_{SFR} decreases as stellar mass increases. However, when imposing a secondary relation with the stellar mass, we do not find a strong reduction in the scatter of the Σ_{SFR}–P_h relation. If the potential of the host galaxy affects the production of stars at kpc scales, its effect is rather mild.

(v) The Σ_{SFR}–P_h relation does not seem to be affected by the host galaxy's morphological type. Furthermore, central regions in barred galaxies have similar $4\,P_h/\Sigma_{SFR}$ ratios than those located in the centre of disc galaxies. In the framework of feedback from recently formed stars, this suggests that bars may play a secondary role as a source of pressure support in late-type galaxies.

Our results indicate that, thanks to the self-regulation of the star formation, the mid-plane pressure plays a paramount role in shaping the creation of newly born stars at kpc scales in disc galaxies. Injection of momentum flux from supernovae explosions to the ISM is apparently one of the main processes that induce this self-regulation. However, our analysis, in agreement with previous studies, also suggests that there can be another process that can support the pressure in disc galaxies. Numerical simulations exploring these different channels are thus required as well as spatially resolved observations in actively star-forming regions.

ACKNOWLEDGEMENTS

We thank the referee for useful comments that improve the quality of this study. JB-B and SFS acknowledge support from the grants IA-100420 and IN100519 (DGAPA-PAPIIT ,UNAM) and funding from the CONACYT grants CF19-39578, CB-285080, and FC-2016-01-1916. SV, ADB, RCL, and VVL acknowledge partial support from NSF – AST1615960. TW, YC, and YL acknowledge support from the NSF through grant AST-1616199. DC acknowledges support from the *Deutsche Forschungsgemeinschaft*, DFG, project number SFB956A.

DATA AVAILABILITY

As we mention in Section 2.2, the data used to derive the physical quantities presented in this paper are those available in the `edge_pydb` data base. A detailed description of the data base can be found in Wong et al. (in preparation).

REFERENCES

Barrera-Ballesteros J. K. et al., 2016, MNRAS, 463, 2513
Barrera-Ballesteros J. K. et al., 2020, MNRAS, 492, 2651
Barrera-Ballesteros J. K. et al., 2021, ApJ, 909, 131B
Benincasa S. M., Wadsley J., Couchman H. M. P., Keller B. W., 2016, MNRAS, 462, 3053
Bigiel F., Blitz L., 2012, ApJ, 756, 183
Bigiel F., Leroy A., Walter F., Brinks E., de Blok W. J. G., Madore B., Thornley M. D., 2008, AJ, 136, 2846
Bock D. C. J. et al., 2006, in Stepp L. M., ed., Proc. SPIE Conf. Ser. Vol. 6267, Ground-based and Airborne Telescopes. SPIE, Bellingham, p. 626713
Bolatto A. D. et al., 2017, ApJ, 846, 159
Bolatto A. D., Wolfire M., Leroy A. K., 2013, ARA&A, 51, 207
Caldú-Primo A., Schruba A., Walter F., Leroy A., Sandstrom K., de Blok W. J. G., Ianjamasimanana R., Mogotsi K. M., 2013, AJ, 146, 150
Cano-Díaz M. et al., 2016, ApJ, 821, L26
Cano-Díaz M., Ávila-Reese V., Sánchez S. F., Hernández-Toledo H. M., Rodríguez-Puebla A., Boquien M., Ibarra-Medel H., 2019, MNRAS, 488, 3929
Catalán-Torrecilla C. et al., 2015, A&A, 584, A87
Colombo D. et al., 2018, MNRAS, 475, 1791
Colombo D. et al., 2020, A&A, 644, A97
Cox D. P., 1981, ApJ, 245, 534
Dey B. et al., 2019, MNRAS, 488, 1926
Diemer B. et al., 2019, MNRAS, 487, 1529
Diesing R., Caprioli D., 2018, Phys. Rev. Lett., 121, 091101
Dopita M. A., 1985, ApJ, 295, L5
El-Badry K., Ostriker E. C., Kim C.-G., Quataert E., Weisz D. R., 2019, MNRAS, 490, 1961
Ellison S. L. et al., 2020, MNRAS, 493, L39
Ellison S. L., Sánchez S. F., Ibarra-Medel H., Antonio B., Mendel J. T., Barrera-Ballesteros J., 2018, MNRAS, 474, 2039
Elmegreen B. G., 1989, ApJ, 338, 178
Faucher-Giguère C.-A., Quataert E., Hopkins P. F., 2013, MNRAS, 433, 1970
Fisher D. B., Bolatto A. D., White H., Glazebrook K., Abraham R. G., Obreschkow D., 2019, ApJ, 870, 46
García-Benito R. et al., 2015, A&A, 576, A135
Gentry E. S., Krumholz M. R., Madau P., Lupi A., 2019, MNRAS, 483, 3647
Gong M., Ostriker E. C., Kim C.-G., Kim J.-G., 2020, ApJ, 903, 142, ()
Graham A. W., Driver S. P., 2005, Publ. Astron. Soc. Aust., 22, 118
Heckman T. M., Thompson T. A., 2017, preprint (arXiv:1701.09062)
Heckman T. M., Alexandroff R. M., Borthakur S., Overzier R., Leitherer C., 2015, ApJ, 809, 147
Herrera-Camus R. et al., 2017, ApJ, 835, 201
Hirashita H., Buat V., Inoue A. K., 2003, A&A, 410, 83
Hopkins P. F., Quataert E., Murray N., 2011, MNRAS, 417, 950
Hopkins P. F., Kereš D., Oñorbe J., Faucher-Giguère C.-A., Quataert E., Murray N., Bullock J. S., 2014, MNRAS, 445, 581
Husemann B. et al., 2013, A&A, 549, A87
Ibáñez-Mejía J. C., Mac Low M.-M., Klessen R. S., Baczynski C., 2017, ApJ, 850, 62
Iffrig O., Hennebelle P., 2015, A&A, 576, A95
Jeřábková T., Hasani Zonoozi A., Kroupa P., Beccari G., Yan Z., Vazdekis A., Zhang Z. Y., 2018, A&A, 620, A39
Kennicutt R. C., Jr, 1998a, ARA&A, 36, 189
Kennicutt R. C., Jr, 1998b, ApJ, 498, 541
Kennicutt R. C., Evans N. J., 2012, ARA&A, 50, 531
Kim C.-G., Ostriker E. C., 2015, ApJ, 802, 99
Kim C.-G., Ostriker E. C., 2017, ApJ, 846, 133
Kim C.-G., Kim W.-T., Ostriker E. C., 2011, ApJ, 743, 25
Kim C.-G., Ostriker E. C., Kim W.-T., 2013, ApJ, 776, 1
Kim C.-G., Ostriker E. C., Raileanu R., 2017, ApJ, 834, 25
Kim J.-G., Kim W.-T., Ostriker E. C., 2018, ApJ, 859, 68
Kregel M., van der Kruit P. C., de Grijs R., 2002, MNRAS, 334, 646
Krumholz M. R., Burkhart B., 2016, MNRAS, 458, 1671
Krumholz M. R., McKee C. F., 2005, ApJ, 630, 250
Krumholz M. R., Burkhart B., Forbes J. C., Crocker R. M., 2018, MNRAS, 477, 2716
Lacerda E. A. D. et al., 2018, MNRAS, 474, 3727
Leitherer C., Ekström S., Meynet G., Schaerer D., Agienko K. B., Levesque E. M., 2014, ApJS, 212, 14
Leroy A. K., Walter F., Brinks E., Bigiel F., de Blok W. J. G., Madore B., Thornley M. D., 2008, AJ, 136, 2782
Levy R. C. et al., 2018, ApJ, 860, 92
Lin L. et al., 2019, ApJ, 884, L33
Madau P., Dickinson M., 2014, ARA&A, 52, 415
Marino R. A. et al., 2013, A&A, 559, A114
Martig M., Bournaud F., Teyssier R., Dekel A., 2009, ApJ, 707, 250
Martizzi D., Faucher-Giguère C.-A., Quataert E., 2015, MNRAS, 450, 504
Mejía-Narváez A., Sánchez S. F., Lacerda E. A. D., Carigi L., Galbany L., Husemann B., García-Benito R., 2020, MNRAS, 499, 4838
Murray N., Ménard B., Thompson T. A., 2011, ApJ, 735, 66
Orr M. E. et al., 2018, MNRAS, 478, 3653
Ostriker E. C., Shetty R., 2011, ApJ, 731, 41
Ostriker E. C., McKee C. F., Leroy A. K., 2010, ApJ, 721, 975
Roth M. M. et al., 2005, PASP, 117, 620
Salpeter E. E., 1955, ApJ, 121, 161
Sánchez S. F. et al., 2012, A&A, 538, A8
Sánchez S. F. et al., 2016a, Rev. Mex. Astron. Astrofis., 52, 21
Sánchez S. F. et al., 2016b, Rev. Mex. Astron. Astrofis., 52, 171
Sánchez S. F. et al., 2016c, A&A, 594, A36
Sánchez S. F. et al., 2021, MNRAS, preprint (arXiv:2102.06226)
Sánchez S. F., 2020, ARA&A, 58, 99
Semenov V. A., Kravtsov A. V., Gnedin N. Y., 2017, ApJ, 845, 133
Shetty R., Ostriker E. C., 2012, ApJ, 754, 2
Shi Y. et al., 2018, ApJ, 853, 149
Shi Y., Helou G., Yan L., Armus L., Wu Y., Papovich C., Stierwalt S., 2011, ApJ, 733, 87
Silk J., 1997, ApJ, 481, 703
Sun J. et al., 2020, ApJ, 892, 148
Thompson T. A., Quataert E., Murray N., 2005, ApJ, 630, 167
Utomo D. et al., 2017, ApJ, 849, 26
van der Kruit P. C., 1988, A&A, 192, 117
Walch S., Naab T., 2015, MNRAS, 451, 2757
Walcher C. J. et al., 2014, A&A, 569, A1
Wang J. et al., 2014, MNRAS, 441, 2159
Wuyts S. et al., 2011, ApJ, 742, 96
Zheng Z., Meurer G. R., Heckman T. M., Thilker D. A., Zwaan M. A., 2013, MNRAS, 434, 3389

APPENDIX A: ESTIMATION OF l_S

In Section 2.3, we derive $\sigma_{*,z}$ by adopting a relation between the scale height, h_s, and the stellar scale length, l_s. This stellar scale length has been measured for this sample of galaxies (Bolatto et al. 2017, Villanueva et al., in preparation). Instead of these measured values, we estimate the scale length as $l_s = R_{\rm eff}/1.68$ (i.e. assuming a Sersic profile with $n = 1$, Graham & Driver 2005). As we mention in Section 2.3, we adopt this value to provide an estimation of l_s in larger samples of galaxies where only $R_{\rm eff}$ has been determined. In Fig. A1 we compare the distribution of the $\sigma_{\rm mol}/\sigma_{\rm stars,\,z}$ ratio using

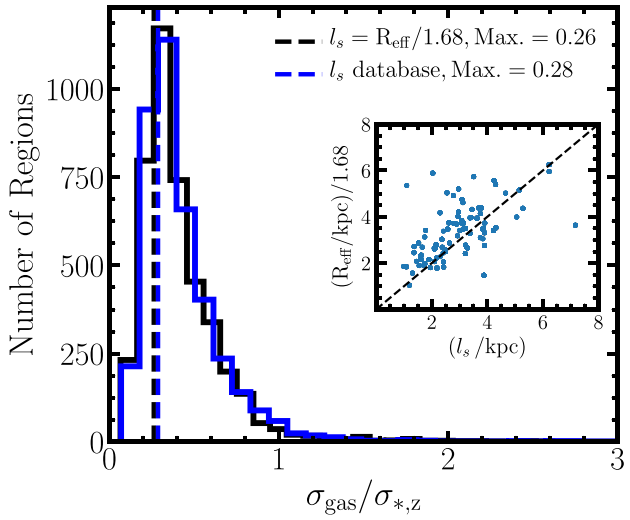

Figure A1. Distribution of the $\sigma_{mol}/\sigma_{stars,\,z}$ velocity dispersion ratio derived for the EDGE-CALIFA survey using the measurements of l_s (blue histogram) and using the adopted value $l_s = R_{eff}/1.68$ (black histogram). The blue and black vertical dashed lines represent the mode of each distribution. Both distribution are quite similar, furthermore the inset shows that the two values (l_s and $R_{eff}/1.68$ are quite similar).

the measurement of l_s included in the `edge_pydb` data base (blue histogram) and the distribution using the value of l_s adopted in this study (black histogram). We find little difference between these two distributions. The mode of both distribution is very similar (~ 0.27). In the inset of Fig. A1, we compare l_s measured and $R_{eff}/1.68$. These values tend to follow the unity slope.

APPENDIX B: ESTIMATE OF THE Σ_{SFR}–P_H RELATION FROM SCALING RELATIONS

As we mention in Section 3.2, Σ_{SFR}, Σ_*, and Σ_{gas} are closely correlate with each other (Lin et al. 2019). Sánchez et al. (in preparation) derive similar scaling relation using the EDGE-CALIFA data set. Using those scaling relations we derive in this section the Σ_{SFR}–P_h relation. In Section 3.2, we present those scaling relations (equations 7–9). To derive our set of measurements, first we define Σ_* as a set of 2×10^4 values that follow the distribution of the observed stellar density (see Sánchez et al. for details). This distribution peaks at $\sim 10^2$ $M_\odot$ pc^{-2}with a dispersion of $\sim$0.4 dex. Then, using these values of Σ_*, we derive Σ_{SFR} from equation (8) and Σ_{mol} from equation (9). We also derive Σ_{SFR} from equation (7) using these values of Σ_{mol}. We perturb these measurements by adding random noise within a scatter in agreement with the typical uncertainties of each measurement (i.e. 0.15, 0.28, and 0.20 dex for Σ_*, Σ_{mol}, and Σ_{SFR}, respectively). The fiducial values of Σ_{SFR} used in this test are the average of those obtained in equations (8) and (7). In the top panels of Fig. B2, we show the scaling relations derived in this test.

Using these values of Σ_* and Σ_{mol}, we derive P_h from equation (1). Following the results from Appendix A, we use the distribution in Fig. A1 to random assign the $\sigma_{mol}/\sigma_{stars,\,z}$ ratio. In Fig. B1, we show the Σ_{SFR}–P_h relation from this mock data set. We follow the same procedure as in Section 3.1 to derive the best fit to this relation. To compare with the measured Σ_{SFR}–P_h relation we overplot the contours from Fig. 2 as well as the best relation derived in Section 3.1. The bulk of the distribution from the mocked data set agrees with

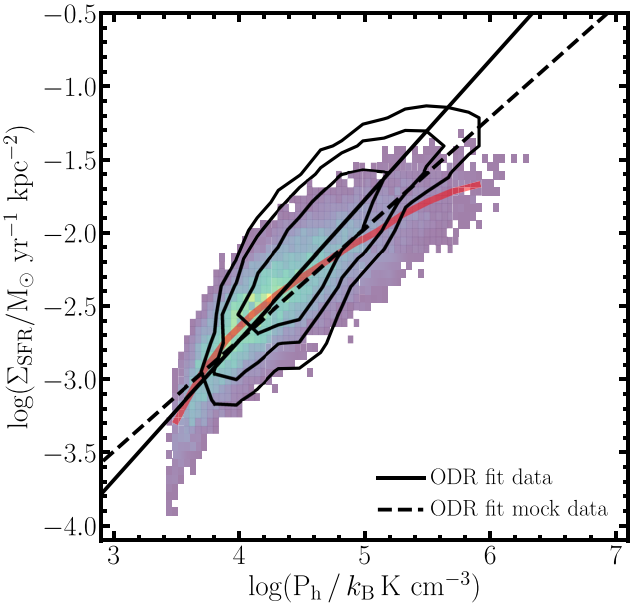

Figure B1. The Σ_{SFR}–P_h relation derived from the scaling relations presented in Sánchez et al. 2021for the EDGE-CALIFA sample colour-coded by the density of points (see details in Appendix B). The red line shows the average Σ_{SFR} for different bins of P_h. The contours are the same as those in Fig. 2. The black solid line represents the best fit derived from the observed data set. The black dashed line represents the best relation derived in Section 3.1.

observations. However, the trend of the Σ_{SFR}–P_h relation from this mock data set is different from the one derived from observations. On the one hand, for the low-pressure regime, these mock data show the drop in Σ_{SFR}, consistent with previous measurements from H I-rich regions (e.g. Leroy et al. 2008). On the other hand, in the high-pressure end, the relation significantly deviates from the best fit derived from the observations. Even more, the best fit from these mock data is sublinear ($b \sim 0.76$ and $\log(A) \sim 0.26$). This test shows that from the local scaling relation there are significant deviations from a linear trend, in particular at the extreme pressures. It also suggests that more mechanisms other than feedback have to be considered in order to properly explain the Σ_{SFR}–P_h. We caution that this is not a definitive test. For instance, we are not sampling the scaling relation for dense/starburst regions where it is very likely that they differ from those derived from typical star-forming regions.

In the bottom panels of Fig. B2, we plot the residuals of the scaling relation derived from equations (7)–(9) against the residuals of the Σ_{SFR}–P_h relation. For each panel, the blue and black contours encloses the sample within approximately 1σ of the mock and observed distributions (see, Fig. 3), respectively. For the star-forming scaling relations (i.e. the rSK and the rSFMS), we find Pearson correlation coefficients among these residuals similar but smaller as those presented in the EDGE-CALIFA data set ($r = 0.86$ and 0.55, respectively). Contrary to the lack of correlation that we derive in Section 3.2, we find in this simulation a significant anticorrelation between the residuals of the rMGMS and the residuals of the Σ_{SFR}–P_h relation ($r = -0.47$).

When we compare the blue and black contours in the bottom panels of Fig. B2 we note that for the left-hand panel, they are very similar. This can be an indication that the correlation between the residuals

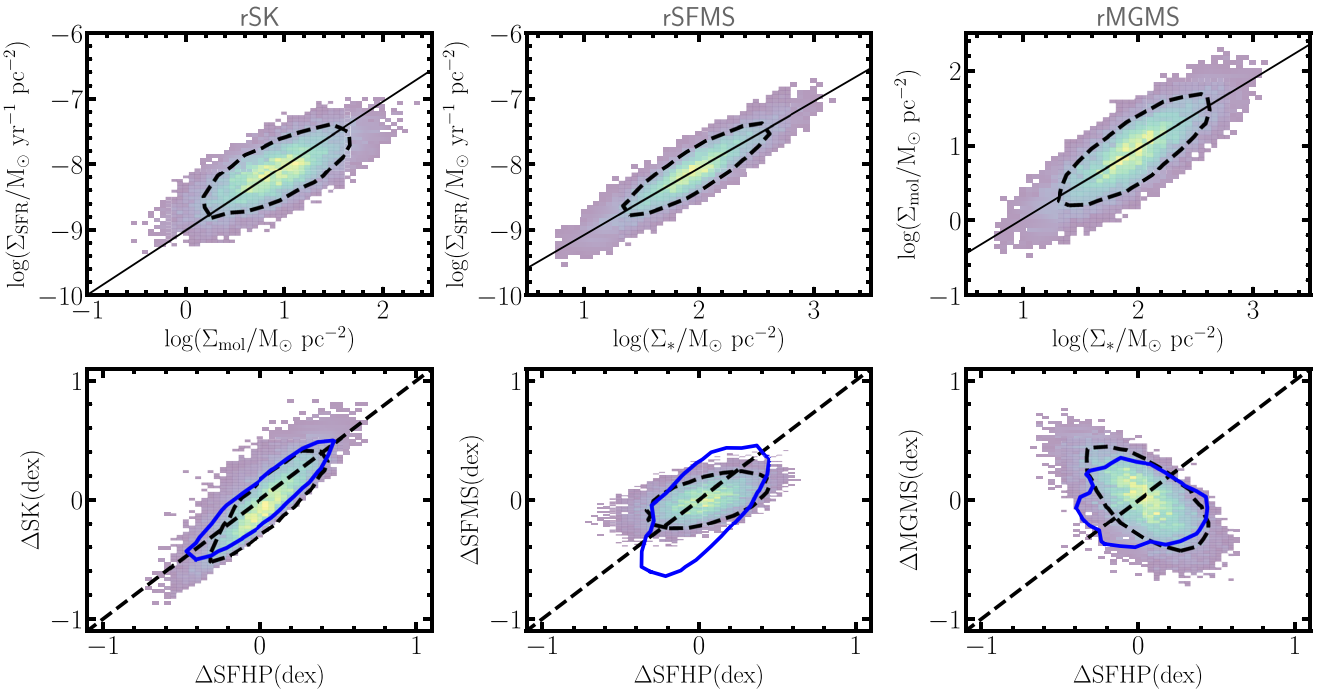

Figure B2. Top panel: mock distributions of the best scaling relations at kpc scales derived from the EDGE-CALIFA sample. From the left- to right-hand side, the Schmidt–Kennicutt relation (rSK), the star formation main sequence (rSFMS), and the molecular gas main sequence (rMGMS). These relations are derived by assuming the relations presented in equations (7)–(9). Bottom panel: the residuals of the scaling relations from the top panels against the residuals from the $\Sigma_{\rm SFR}$–$P_{\rm h}$ relation derived from these scaling relations. In all panels the dashed black contours include ∼68 per cent of the sample, whereas the blue contours in bottom panels represent ∼68 per cent of the sample presented in Fig. 3. The similarity between these distributions allows us to estimate whether they may be induced relations.

of the rSK and the $\Sigma_{\rm SFR}$–$P_{\rm h}$ relation could be induced by statistical errors between these scaling relations, instead of been correlated by a physical driver. For the middle panel, we find that distribution of the residuals of the rSFMS and those from the $\Sigma_{\rm SFR}$–$P_{\rm h}$ relation derived from this simulation are more concentrated around zero than those derived from observations. This, in turn, may suggest that the observed relation of the scatter may have a physical explanation. Finally, from the simulated data set, we are not able to reproduce the lack of correlation between the residuals of the rMGMS and the $\Sigma_{\rm SFR}$–$P_{\rm h}$ relation. This supports the hypothesis that $P_{\rm h}$ is an observable that describes better the $\Sigma_{\rm SFR}$ at kpc scales rather than the gas fraction measured by the residuals of the rMGMS. In a more detailed work, we explore the implications of studying the residuals of the scaling relations at kpc scales (Sánchez et al. 2021).

This paper has been typeset from a TEX/LATEX file prepared by the author.